THE STRUCTURE AND CHEMISTRY OF EPITAXIAL 2D CHALCOGENIDES

A Thesis

Presented to the Faculty of the Graduate School

of Cornell University

in Partial Fulfillment of the Requirements for the Degree of

Master of Science

by

Aditya Sundar

August 2017

ABSTRACT

Molybdenum based transition metal dichalcogenides have drawn widespread attention from the scientific community as they hold high promise in the field of semiconductors and valleytronics. Weak van der Waals (vdW) forces between layers eliminate substrate lattice constraints and allow epitaxial growth on different materials. Alloying the metallic or chalcogen species will potentially allow us access to intermediate structural, optical and electronic parameter space. In this work, we report the molecular beam epitaxial growth of alloyed $MoSe_{2-x}Te_x$ thin films on 3D substrates: CaF_2 and GaAs substrates. Growth at 400°C by co-injection of the chalcogen species results in preferential Se incorporation. By pulsing the chalcogen injection at 340°C, up to 44% Te incorporation is achieved in $MoSe_{2-x}Te_x$. Detailed structural, chemical and optical investigation is used to identify the phase, polytype, chemistry and electronic states of the alloy. Also, the 2D-2D interface between graphene and chalcogenide films is studied to map rotational alignment, strain and mosaicity.

An experiment is a question which science poses to Nature,
and a measurement is the recording of Nature's answer.

– Max Planck

ACKNOWLEDGEMENTS

Working in the group of Prof. Huili (Grace) Xing and Prof. Debdeep Jena has been a tremendous stepping stone in my young research career. The opportunity to perform my Master's thesis research under their guidance has been the most fruitful experience of my life thus far. Prof. Xing's tireless motivation and scientific inquiry and Prof. Jena's motivational teaching are the pillars upon which this research is built.

I specially thank our senior group member Suresh Vishwanath, for growing all samples that were studied in this research, and for the countless discussions we had to resolve difficulties. Experiments at the Cornell High Energy Synchrotron Source would not have seen the light of the day were it not for Dr. Arthur Woll's commitment. His help with experimentation and data processing has been crucial to my progress. I also thank Dr. Vladimir Protasenko for training and constantly guidigng me with the lab infrastructure.

A special round of thanks to Long Yuan at Purdue University (and advisor Prof. Libai Huang) for showing the strengths of collaboration. I also acknowledge Dr. Sergei Rouvimov and the team at the University of Notre Dame for technical insights and knowledge; particularly with transmission electron microscopy. The collaboation with Yu-Chuan Lin at PennState has been crucial in the completion of this project. Low energy electron diffraction results were obtained at Cornell and thanks are due to Edward Lochocki and Prof. Kyle Shen. Discussions and critiques from other group members Rusen Yan, Mingda Li and Brian Schutter have been very important to this research. Contribution and encouragement from my labmates Huai Hsun Lien, Kevin Lee, Liheng Zhang, Nick Tanen, Sam Bader, Shyam Bharadwaj, Wenshen Li, Reet Chaudhuri and Hyunjea Lee has been crucial in keeping me focussed.

TABLE OF CONTENTS

LIST OF TABLES

LIST OF FIGURES

CHAPTER 1

INTRODUCTION

The isolation of a single layer of graphene in 2004 has paved way for the discovery of a plethora of lower dimensional materials. Andre Geim and Konstantin Novoselov's rediscovery of the two dimensional allotrope of Carbon thrust 2D materials into the scientific limelight. Graphene in particular came to be regarded as the wonder materials owing to its tremendous properties: extreme mechanical robustness, exceptional electrical and thermal conductivity and easy chemical functionalisation. Consequently, graphene is expected to improve several technologies ranging from transistors, batteries, catalysts etc. While graphene and other allotropic members of the 2D family like silecene, germanene have intrinsically zero bandgaps that are tunable, there exist many other 2D materials that possess finite bandgaps. This makes them suitable for applications in transistors and solar cells. One such class of layered materials is transition metal dichalcogenides (TMDs). Their chemistry is MX_2, where M is the transition metal and X is the chalcogenide. In the monolayer (ML) form, these materials are known to have a direct bandgap. The versatility of these materials lies in the tunability of their characteristic properties with layer number, strain etc.

These materials are foreseen to have several electronic and chemical applications. They open doors to the field of valleytronics since each of the two energy-degenerate valleys consists of electronic states with one spin orientation. Novel electronic states are accessible at low temperatures due to carrier confinement in two dimensions. Integer Hall effect, spin-valley coupling, Majorana fermions have been observed in TMD materials. Larger surface areas and vdW gap between provide increased interfaces for surface functionalisation. This presents

new opportunities in purification and gas detection. Most of the initial research was pioneered by mechanical exfoliation of these materials from the bulk. Weak van der Waals interaction perpendicular to the 2D layer allows easy separation of the layers by mechanical means. While using a scotch tape or polymer stamps (poly(methly methacrylate), polydimethylsiloxane) has proven to be very efficient in stacking homo/heterostructural layers, the technique comes with its drawbacks. Exfoliating from bulk offers very little control over shape and thickness. Repeatability of measurement is its Achilles heel. This brings us to epitaxial growth which offers precise control over thickness, doping and properties. Following initial success in the Chemical vapour depostion (CVD) of graphene on Cu, Ni, Pd etc, TMD materials were grown on SiO_2, $\alpha - Al_2O_3$ etc. Key questions to address in epitaxy include the mode of crystal growth, impact of substrate on properties and detachment of film from the substrate.

CHAPTER 2

$MoSe_{2-x}Te_x$ alloys by molecular beam epitaxy

2.1 Literature

Layered transition metal dichalcogenides (TMDs) are currently widely investigated for interesting physics and applications[6, 7, 8, 9]. Notably, $MoTe_2$ has a semiconducting phase and metallic phase[10, 11]. The semiconducting phase is interesting because of its smallest bandgap[12] among all molybdenum chalcogenides [13] in the monolayer limit[12]. It also has type III (broken) band alignment with $SnSe_2$[14], ideal for tunneling applications such as Esaki diodes[15] and Two-dimensional heterostructure interlayer tunnelling field effect transistor (Thin-TFET)[16]. Molecular beam epitaxy (MBE) grown $MoSe_2$ [17, 18, 8, 19, 20, 21, 22], $MoTe_2$ [20, 23] and their heterostructures [24] have been studied by several groups recently.

Our group has published one of the earliest reports on the MBE growth of $MoSe_2$ on CaF_2 and graphene[18]. Low temperature electrical transport by variable range hopping has been observed in MBE $MoSe_2$ and $MoTe_2$ on sapphire substrates[20]. As a natural progression, there have been few efforts to realise alloyed TMDs. Here is an example of alloyed bulk 2D materials. $Mo_{1-x}W_xSe_2$ grown by chemical vapour transport (CVT) were shown to possess composition dependent Raman shifts and PL emission energies[25]. The in plane (E^1_{2g}) and out of plane (A_{1g}) modes both exhibited shifts as x was varied between 0 and 1. Elemental mapping of Mo, W and Se from scanning transmission electron microscopy (STEM) indeed revealed an alloyed nature with all elements randomly distributed. Similar raman shifts were reported in CVT $Mo_{1-x}W_xS_2$ [26].

For device applications, it is essential to control the optical and electronic properties of any semiconductor. Modulation of the optical band gap was demonstrated in $MoS_{2-x}Se_x$ [27]. Selenization of MoS_2 was achieved by introducing vapourized Se over MoS_2 in a CVD chamber. The bandgap of pristine monolayer (ML) MoS_2 (1.86 eV) was changed up to 1.57 eV by chalcogen substitution. $MoSe_{2-x}Te_x$ growth on HOPG and MoS_2 was very recently demonstrated by van der Waals epitaxy[28]. This was achieved by co-deposition of Se and Te at 300°C, with the chalcogen flux being 10 times higher than the Mo flux. ARPES measurements on $MoSe_{1.8}Te_{0.2}$ revealed valence band maxima (VBM) features at Γ similar to $MoSe_2$. Core level binding energies examined by synchrotron photoemission showed differences in the Se-3d doublet peaks for $MoSe_2$ and $MoSe_{1.8}Te_{0.2}$. In this work, we demonstrate the MBE growth of $MoSe_{2-x}Te_x$ on CaF_2 and GaAs by MBE.

2.2 $MoSe_{2-x}Te_x$ on CaF_2

In this work, we report the growth of chalcogen alloyed $MoSe_{2-x}Te_x$ by MBE. We investigate films grown under chalcogen co-injection and short-period superlattice (SPS) growth (by pulsing the chalcogen fluxes). Using sub monolayer SPS, we demonstrate up to 44% Te incorporation in $MoSe_{2-x}Te_x$.

2.2.1 Growth conditions

The first series (Series A) contains 3 samples which are $MoSe_2$, $MoSe_{2-x}Te_x$ by co-deposition of Se and Te with two different Se:Te ratios (2.0 and 0.5). These

samples are labelled A1, A2 and A3 respectively in future discussions. All samples in Series A were grown at 400°C and the co-deposited alloying was done by maintaining the total chalcogen flux at a constant value of ~2.5x10^{-6} Torr. The second series (Series B) also contains 3 samples: SPS of $MoSe_2$ and $MoTe_2$ with 3 different time periods of 1:2 (MoSeTe 1:2), 1:1 (MoSeTe 1:1) and 2:1 (MoSeTe 2:1), labelled B1, B2 and B3 respectively. All samples in Series B were grown at 340°C. The Te flux is ~6x10^{-6} Torr and the Se flux is ~3x10^{-7} Torr. All the growth details are listed in tables 2.1 and 2.2.

In our previous publication[18], we have demonstrated the MBE growth of 2H-$MoSe_2$ at 400°C. We also observe that $MoTe_2$ crystallises in the 1T phase at 400°C. A lower temperature of 340°C is required to grow 2H-$MoTe_2$. It was hence decided to grow series B samples at 340°C.

Sample ID	Substrate (Temp)	Growth duration	Growth rate ML/min
A1	CaF_2 (400°C)	45 mins	0.3
A2	CaF_2 (400°C)	45 mins	0.26
A3	CaF_2 (400°C)	45 mins	0.26
B3	CaF_2 (340°C)	$\left(\begin{array}{c}60\text{ sec }MoSe_2\\+\ 30\text{ sec }MoTe_2\end{array}\right)$ x 30	0.13
B2	CaF_2 (340°C)	$\left(\begin{array}{c}30\text{ sec }MoSe_2\\+\ 30\text{ sec }MoTe_2\end{array}\right)$ x 40	0.45
B1	CaF_2 (340°C)	$\left(\begin{array}{c}30\text{ sec }MoSe_2\\+\ 60\text{ sec }MoTe_2\end{array}\right)$ x 30	0.13
C1	n+ GaAs (340°C)	$\left(\begin{array}{c}30\text{ sec }MoSe_2\\+\ 30\text{ sec }MoTe_2\end{array}\right)$ x 60	0.16

Table 2.1: This table lists the substrate temperature and growth times for the samples discussed in this section.

Sample ID	Post growth anneal in chalcogen(s)	Flux ratios		
		Se:Mo	Te:Mo	(Se+Te):Mo
A1	3 mins at 500°C + 7 mins at 600°C	66.3	0	66.3
A2	3 mins at 500°C + 7 mins at 600°C	62	31.3	93.3
A3	3 mins at 500°C + 7 mins at 600°C	35.2	76.5	111.7
B3	3 mins at 450°C + 7 mins at 550°C	21.4	496.4	517.8
B2	3 mins at 450°C + 7 mins at 550°C	6.3	24.5	30.8
B1	3 mins at 450°C + 7 mins at 550°C	20.6	455.1	475.7
C1	3 mins at 450°C + 7 mins at 550°C	79.1	237.4	316.5

Table 2.2: Annealing conditions and calculated fluxes are listed in this table.

2.2.2 X-ray diffraction and reflectivity

ω-2θ scans were used to evaluate the lattice constants of the materials along the out of plane direction. Figure 2.3 represents the (002) peaks for all the films. The 2θ positions for A1, A2 and A3 are calculated to be identical (13.52°). We calculate the c-axis lattice constants of these 3 films to be 13.08 , which is close to the reported value of 13.00[20] for $MoSe_2$. XRD is unable to detect any structural change in the samples in Series A. This suggests that there is no Te incorporation into the lattice. As a preliminary signature of alloyed Se and Te, we find that the (002) XRD peaks for the B1, B2 and B3 lie between reported values for $MoSe_2$ and $MoTe_2$. The films peaks are depicted in Figure 2.3 (d). From the spacing of the fringes in Figure 2.3 (c), it is inferred that Mo(SeTe) 1:1 is thicker than Mo(SeTe) 1:2 and Mo(SeTe) 2:1. The (111) and (222) peaks from CaF_2 are seen at 2θ = 28.26° and 58.47° respectively. We also ran simulations for the (002)

diffraction peak using GlobalFit sofware to understand the observed patterns.

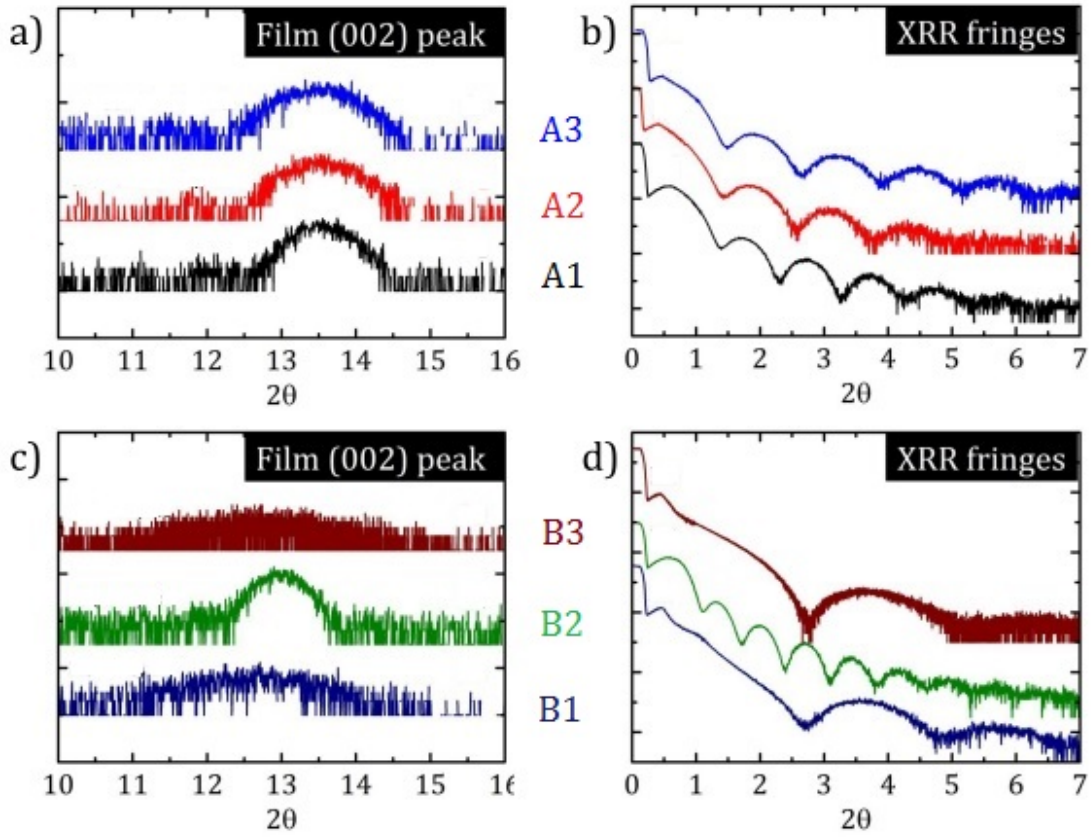

Figure 2.1: (a & b) X-ray reflectivity fringes used to determine the thicknesses of the films. (c & d) $\omega - 2\theta$ scans around (002) peaks.

2.2.3 Raman Spectroscopy

Consistent with the XRD results, the peak positions for A1, A2 and A3 are identical. We observe the A_{1g} peak at 240 cm^{-1} for these 3 samples. The E^1_{2g} peaks are located at 284.50 cm^{-1}-285 cm^{-1}. In agreement with this, the B^1_{2g} peaks for are observed at ~350 cm^{-1} (all corresponding to $MoSe_2$). Again, there is no signature of alloying for the samples in Series A. The FWHM of the A_{1g} peaks for

Film	ID	2θ (002)	Calc. c ()	Thickness ()	# lay.
$MoSe_2$	A1	13.52 ± 0.55	13.08	92.63 ± 1.15	7
MoSeTe co 5:2	A2	13.52 ± 0.55	13.08	79.92 ± 1.39	6
MoSeTe co 1:2	A3	13.51 ± 0.55	13.09	78.65 ± 1.35	6
MoSeTe 2:1	B3	12.72 ± 0.62	13.90	39.58 ± 1.23	3
MoSeTe 1:1	B2	12.99 ± 0.59	13.61	126.51 ± 0.74	9
MoSeTe 1:2	B1	12.59 ± 0.63	14.04	44.93 ± 1.88	3
$MoTe_2$			14[20], 14.4		

Table 2.3: Film thicknesses and c-axis lattice constants calculated from XRR and (002) peak diffraction data.

A1, A2 and A3 are between 4.38 cm^{-1} and 6.07 cm^{-1}. Results thus far indicate that the film crystallises in the 2H phase, which is expected from our previous work on $MoSe_2$[18]. We observe that the peaks for B1, B2 and B3 are red shifted from the $MoSe_2$ peak. It is to be noted that the frequencies decrease progressively with increasing Te concentration (as would be the case for an alloyed material). Peaks for 2H-$MoTe_2$ have been reported at 171-174 cm^{-1} (A_{1g}) and 233-236 cm^{-1} (E^1_{2g} [20, 29, 30]). This corroborates results from XRD as the signals obtained from the alloyed samples lie in between those from $MoSe_2$ and $MoTe_2$. The A_{1g} and E^1_{2g} peak positions follow the same trend as the Te content in the alloys. Increasing Te% results in higher red shifts for these Raman peaks. The B^1_{2g} peak for B3 is also red shifted from the same peak for B1. We however do not observe this peak for B2. This is mostly because of the film being several layers thicker and the B^1_{2g} signal is predicted to be inactive in bulk TMD materials[31, **?**, 32, 33, 34]. The FWHM of the fit peaks are much larger than those observed for the samples in Series A. With increasing Te content, both A_{1g} and E^1_{2g} peaks are found to broaden. The exact FWHM values for all samples are listed in SI table II. Chemical composition dependence of A_{1g} Raman mode and PL emission signals has been observed in $Mo_{1-x}W_xSe_2$ grown by CVT[25]. The red shift in the Raman peaks isn't entirely attributed to Te alloying. The

difference in thickness of the films in Series B is also expected to determine the peaks positions.

It is likely that disorder due to alloying is causing the peaks to broaden.

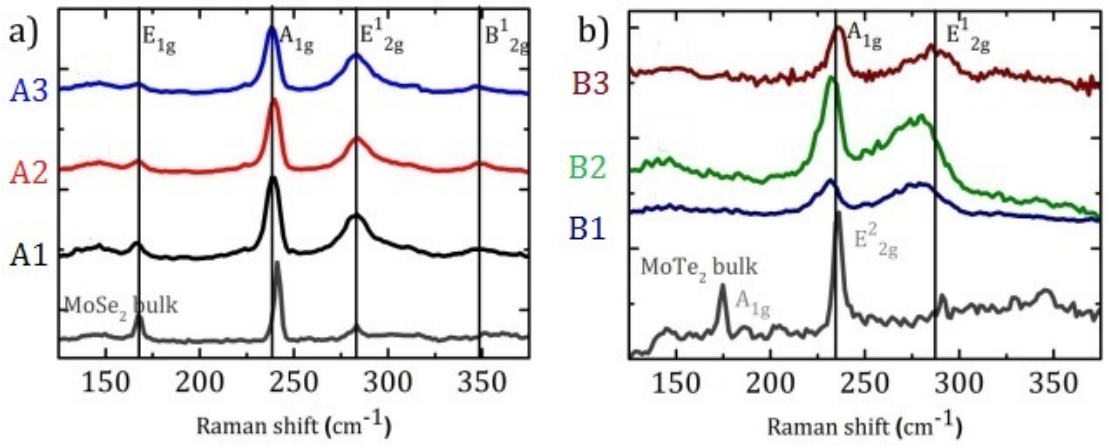

Figure 2.2: (a) Samples A1, A2 and A3 are identified to be $MoSe_2$ from. All the samples are identified to be $MoSe_2$ from their raman spectra. (b) A red shift in the peak positions (towards the $MoTe_2$peak) is observed for samples B1, B2 and B3 indicating Te incorporation.

2.2.4 X-ray Photoelectron Spectroscopy

XPS allows us to chemically distinguish the samples grown by two different growth methods. The Mo-3d, Se-3d and Te-3d energy ranges have been investigated and used to quantify the spectra. Survey scans for A1 and B2 are included in appendix Figure A.4.

In this paragraph, we describe the key features of the samples in Series A. The Mo $3d_{3/2}$ and Mo $3d_{5/2}$ peaks for A1, A2 and A3 are located at binding energies of 231.89 eV and 228.76 eV respectively. The $Mo3d_{5/2}$ peak for epitaxial $MoSe_2$ has been reported at binding energies of 228-229 eV previously[20, 21, 35]. The

Se spectra are also identical for these samples. We observe characteristic Se $3d_{3/2}$ and Se $3d_{5/2}$ peaks at binding energies of 55.22 eV and 54.37 eV respectively. These results also indicate that all samples in series A are $MoSe_2$. Additionally, the Se-3s peak is observed in the Mo-3d scan range. Both Mo and Se show oxidation signals at higher binding energies as compared to their TMD peaks. The relative intensities of the oxide signal to the TMD signal are very low, ~3-4% for all samples. However, there is no detectable Te signal from A2. The presence of Te in A3 is chemically identified by Te $3d_{3/2}$ and Te $3d_{5/2}$ peaks at 572.95 eV and 583.34 eV respectively. Elemental ratios calculated from the integrated intensities are 2.1 (Se:Mo) for A1 & A2 and 1.85(Se):0.06(Te):1(Mo) for A3. These establish the near stoichiometric nature of the 3 films in Series A . The exact numbers are listed in table III in the SI. For this calculation, the area of the Se-3s peak from the Mo-3d signal window has been excluded. XPS studies for samples in series B indicate significant Tellurium incorporation which confirms the growth of alloyed $MoSe_{2-x}Te_x$ growth. The nature of the Mo $3d_{3/2}$ and Mo $3d_{5/2}$ is identical to the non-alloyed samples in Series A. Strong Te $3d_{3/2}$ and Te $3d_{5/2}$ signals are observed for all samples. We interestingly report enhanced oxidation Mo and Se in the presence of Te (along with oxidation of Te). Samples without Te in series A were seen to have much weaker oxidation peaks for Mo and Se. Te likely promotes the oxidation of other elements by drawing more O to the film. It is to be noted that B1 & B3 were grown on the same day, whereas B2 was grown 51 days earlier. Although XPS on the 2:1 and 1:2 samples was done on the same day, under identical conditions, XPS shows greater oxidation of Mo and Se for B1 as compared to B3. Increased presence of Te is seen to promote the oxidation of both Mo and Se. The samples were exposed to atmosphere only during the measurements. At all other times, they were stored

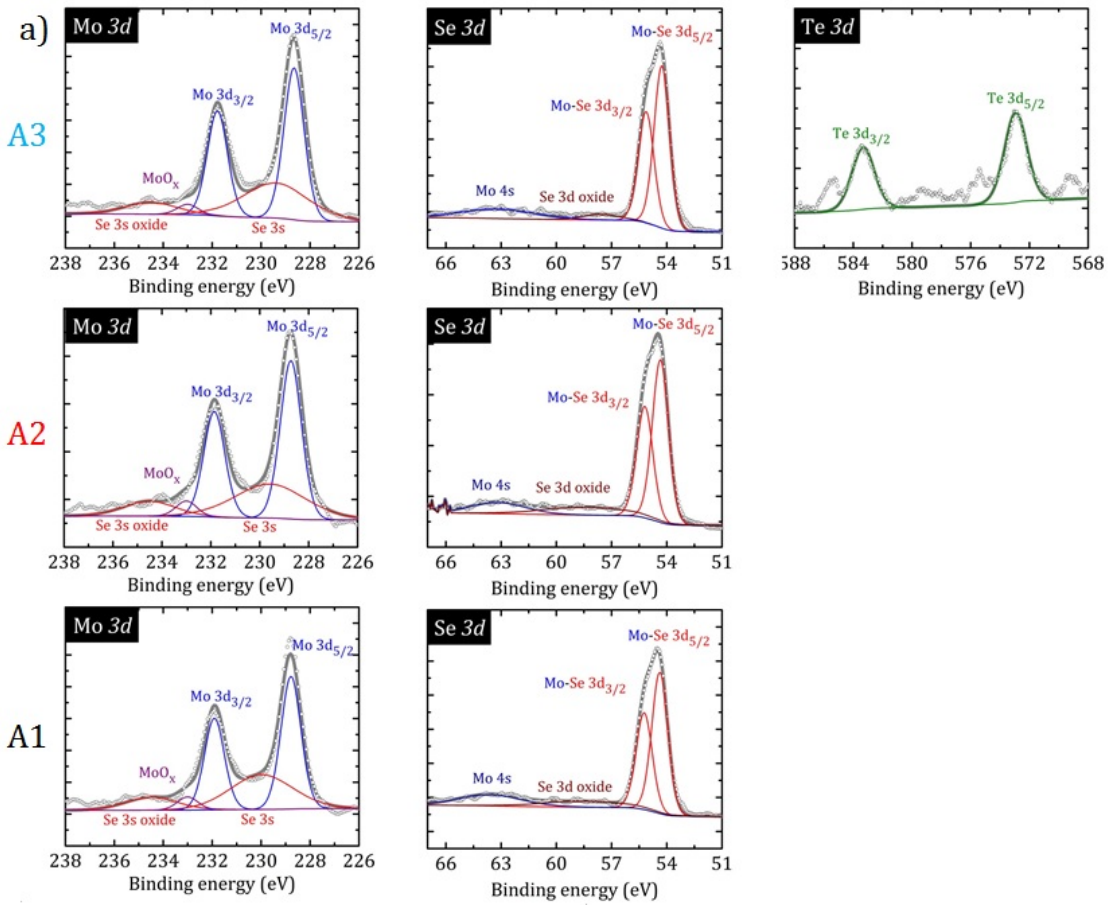

Figure 2.3: Mo-3d, Se-3d and Te-3d XPS spectra for A1 (top row), A2 (middle row) and A3 (bottom row) respectively. All samples have identical Mo and Se spectra. A3 has a weak Te signal, which is absent in A2.

in a container purged with Nitrogen gas. The stoichiometric values for all the samples discussed here are shown in table 2.4. The values are calculated after including the oxide peaks.

2.2.5 Transient Absorption

All data in this subsection were obtained and analyzed at Purdue University by Long Yuan and Prof. Libai Huang in the Department of Chemistry.

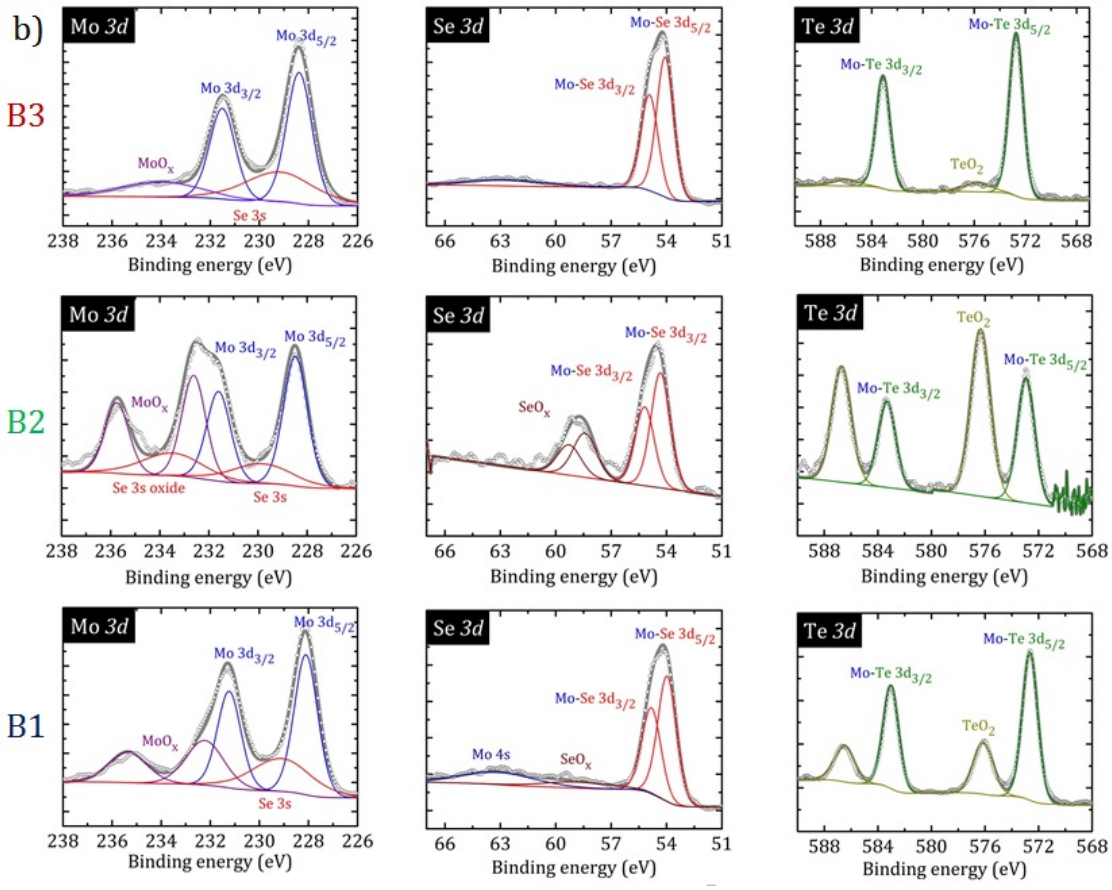

Figure 2.4: Mo-3d, Se-3d and Te-3d XPS spectra for B1 (top row), B2 (middle row) and B3 (bottom row) respectively. All elements show significant oxide peaks indicating enhanced oxidation in the presence of Te.

Femtosecond transient absorption measurements also provide different spectral signatures for the two sets of samples. Figure 2.5 (a1) shows spectrum of series A at a pump-probe delay of 100 fs with 400 nm (3.1 eV) excitation and visible probe (450 - 850 nm). In A1 (black line), we could identify three negative ΔA features which are attributed to the exciton bleach of $MoSe_2$ due to the reduction of absorption on excitation. The bleach energies are around 800 nm (A, 1.55 eV), 700 nm (B, 1.77 eV), and 515 nm (C, 2.41 eV), respectively, which are

Sample	Mo	Se	Te	%Te
A1	1	2	0	0
A2	1	2	0	0
A3	1	1.85	0.06	3.14
B3	1	1.43	0.42	22.70
B2	1	1.14	0.65	36.31
B1	1	1	0.79	44.13

Table 2.4: Atomic ratios calculated from the XPS signals. These were calculated using CasaXPS Version 2.3.17PR1.1 by considering the integrated intensities from only the relevant TMD signal. A1, A2 and A3 stoichiometric in nature in contrast to B1, B2 and B3 which are found to be chalcogen deficient.

consistent with previous reported absorption resonance energies in few layer exfoliated $MoSe_2$[36, 37]. Exciton energies for bulk TMDs[38, 39] agree with our measured values. The A and B exciton resonances originate from the transition between spin-orbit splitting of valence band and degenerated conduction band[40, 41, 42]. The C exciton resonance is attributed to the transition between parallel bands near Γ point of the Brillouin zone which is also well known as the band nesting effect[43]. Spin-orbit energy calculated from as Δ_{AB} from the A and B exciton energies is equal to 220 meV, close to reported values[44, 45]. As depicted by the red curve in Figure 2.5 (a1), the exciton resonance energies observed for A2 are very similar to those seen in A1. TA spectrum for A3 (blue line) depicts three exciton resonance features which originate from $MoSe_2$, but demonstrate a red shift of both A and B exciton bleach with an energy difference around 30 meV. The change of bleach energy in A3 sample provides a direct evidence for controlling exciton properties of $MoSe_2$ through few% Te alloying (XPS signal amounts to ~3%). We also carried out transient dynamics measurements by probing B exciton resonance for these samples (Figure 2.5 (a2)). For A1, the exciton dynamics can be fitted with bi-exponential function convoluted with experimental response function with a fast component of 0.62 ± 0.02 ps

(89.1%) and 46.7 ± 8.2 ps (10.9%) ps as shown in Table 1. A2 exhibits identical decay dynamics to A1. However the decay dynamics in A3 is significantly different to $MoSe_2$ and is fit with a single exponential function convoluted with experimental response function with a decay constant of 0.54 ± 0.01 ps (100%). Our results demonstrate that the incorporation of Te could also notably alter the exciton dynamics of $MoSe_2$. The actual excitonic transitions A, B and C have been described using a band diagram in appendix Figure A.2.

Figure 2.5 (b1) shows transient absorption spectrum for the alloyed films B1 and B2. The 3rd sample discussed here is $MoTe_2$. Growth and other characterisation results for this particular sample can be found in another manuscript[46]. In $MoTe_2$, as shown by the bright green curve, we could identify three exciton bleaches the visible light probe range (450 nm - 850 nm). The bleach energies are ~ 700 nm, 625 nm and 520 nm respectively, which are assigned to excitonic transitions of A′ (1.77 eV), B′ (1.98 eV), and C (2.38 eV) according to previous reflection measurements[47]. The A′ and B′ are attributed to the higher energy levels of the A and B exciton transitions[42, 47]. The C exciton resonance arises from the band nesting effect which mirrors our observation in $MoSe_2$. Since the bandgap at the K point is greater for $MoSe_2$ than for $MoTe_2$, the C exciton is expected to shift to higher wavelengths with Te addition. The dynamics probing at exciton resonance B′ shows a single exponential decay with a decay constant of 0.55 ± 0.07 ps. As shown in Figure 2.5 (b1), we observe B′ and C exciton bleaches in the alloyed sampled B1 and B2, but the A′ exciton bleach is absent. The transient dynamics for B1 and B2 probed at B′ have recombination constants comparable to $MoTe_2$. Their respective decay constants are 0.57 ± 0.06 ps (100%) and 0.45 ± 0.03 ps (100%) . The optical properties of B1 and B2 are quite

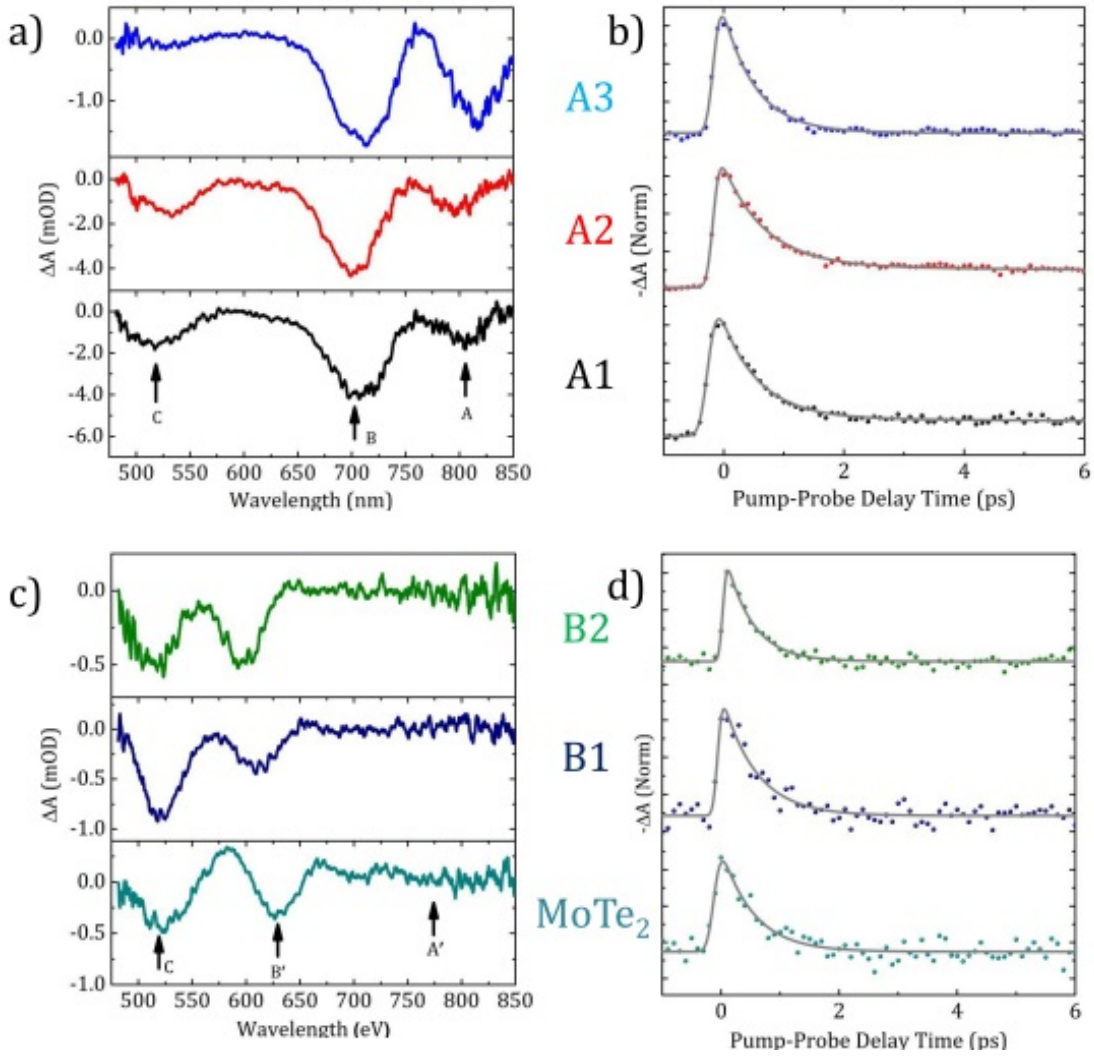

Figure 2.5: .(a1) Bleach energies are observed around 800 nm (A, 1.55 eV), 700 nm (B, 1.77 eV), and 515 nm (C, 2.41 eV) for samples A1 and A2. The energies for A3 are red shifted which might be due to few% Te. (a2) Transient dynamics for exciton resonance B fitted with exponential function convoluted with experimental response function. (b1) Bleach energies are around 700 nm (A', 1.77 eV), 625 nm (B', 1.98 eV), and 520 nm (C, 2.38 eV) for B1, B2 and and $MoTe_2$. (b2) Transient dynamics for exciton resonance B' fitted with single exponential function convoluted with experimental response function.

similar to $MoTe_2$. The oxidation of Mo and Se in Te rich samples (as seen in the previous section) can cause the alloyed samples 1:1 to behave more like $MoTe_2$.

Sample	τ_1 (ps)	τ_2 (ps)
A1	0.62 ± 0.02 (89.1%)	46.7 ± 8.2 (10.9%)
A2	0.71 ± 0.02 (86.2%)	44.5 ± 4.9 (13.8%)
A3	0.54 ± 0.01 (100%)	N.A.
B2	0.45 ± 0.03 (100%)	-
B1	0.57 ± 0.06 (100%)	-
$MoTe_2$	0.55 ± 0.07 (100%)	-

Table 2.5: Fitting parameters for exciton dynamics probe at B bleach in series A and B. A1 and A2 can be fit with a bi-exponential function whose decay time constants are listed as τ_1 and τ_2. However, A3 is fit using a single exponential function.

2.3 $MoSe_{2-x}Te_x$ on GaAs

TEM results were acquired and analysed by Dr. Sergei Rouvimov at the University of Notre Dame. XPS and LEED in this section was done at Cornell University by Edward Lochocki, guided by Prof, Kyle Shen. Our studies on samples grown on $CaF2_2$ confirm the presence of Se and Te in the films. The dependence of optical properties on Te content is indicated by spectral shifts in diffraction and spectroscopy measurements. However, oxidation in the ambient is a significant deterrent to study the local structure of the alloy. To circumvent this, a $MoSe_{2-x}Te_x$ 1:1 sample was grown on GaAs. GaAs was used as disintegration of CaF_2 under e^- beam renders it infeasible for electron microscopy. The sample was capped with Se in situ. For all measurements described in this section, the Se was decapped in UHV to minimise oxidation

2.3.1 TEM, LEED and XPS

Cross sectional TEM was done to study the local structure of the alloyed sample. From 2.6 (a), it is seen that the $MoSe_{2-x}Te_x$ is epitaxially grown on the n+GaAs substrate. At this resolution, we do not observe any intensity changes in the film region which suggests that the film is not phase segregated. The $MoSe_{2-x}Te_x$ film is ~7 layers thick. Also, LEED spots reflect a 6-fold symmetric structure with a lattice constant of 3.32 in the plane. This is greater than the value of 3.25 that we reported for $MoSe_2$ grown on CaF_2. This could potentially be due to Te incorporation but the lattice parameter of $MoSe_2$ has been reported to change based on the growth method, substrate and charaterisation technique (compared in SI table III). Energy dispersive X-ray spectroscopy also shows that the film contains Mo, Se and Te atoms. XPS spectra obtained from these samples

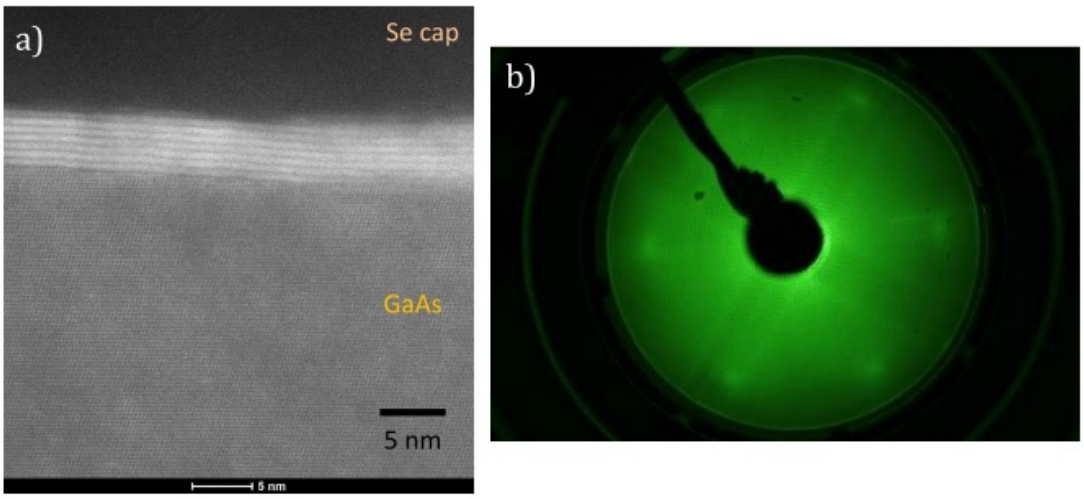

Figure 2.6: a) HAADF STEM showing epitaxial growth of $MoSe_{2-x}Te_x$. (b) LEED showing hexagonal symmetry of $MoSe_{2-x}Te_x$.

also indicate that $MoSe_{2-x}Te_x$ might be locally alloyed. As depicted in Figure 2.7 (a), the Mo-3d peak from $MoSe_{2-x}Te_x$ is found to have binding energies be-

tween the corresponding values for 2H-$MoSe_2$ and 2H-$MoTe_2$. It was difficult to draw such an observation from the samples on CaF_2 since oxide peaks can case additional shifts in the binding energy. The composition is calculated to be $MoSe_{1.63}Te_{0.27}$ which is close to the expected dichalcogenide value but Se rich. Doublet spectral components for this sample are not shown here for clarity. This is included in appendix Figure A.5. Oxide components were not observed for any of the elements.

While LEED can confirm the hexagonal surface, the polytype is not known as both 2H and 1T have hexagonal in-plane structures. Extended x-ray absorption fine structure (EXAFS) is ideally suited to probe the crystal structure of the material. Bond length calculations derived from EXAFS on this samples also support our earlier observations. The polytype is estalished to be 2H and bond elongations (from $MoSe_2$) is suggestive of Te incorporation. These results are discussed in the next subsection.

2.3.2 X-ray Absorption Spectroscopy

$$\chi\left(\mathrm{q}\right) \propto \sum_{\mathrm{j}} \mathrm{N_j} \frac{\mathrm{t_j}\left(\mathrm{q}\right) * \sin\left(2\mathrm{qR_j} + \delta_{\mathrm{j}}\left(\mathrm{q}\right)\right)}{\mathrm{R_j^2}} \mathrm{e}^{-2\left(\mathrm{q}\sigma_{\mathrm{j}}\right)^2} \mathrm{e}^{\frac{-2\mathrm{R_j}}{\Lambda}}$$

$\chi\left(\mathrm{q}\right) = \frac{\mu_{\mathrm{x}}(\mathcal{E}) - \mu_0(\mathcal{E})}{\mu_0(\mathcal{E})}$ (1) is the normalised absorption. q is the wave vector at energy $\mathcal{E}$, μ_{x} is the absorption coefficient for the atom in a crystal and μ_0 is the absorption coefficient for the same atom in vacuum. The central absorption atom is surrounded by $\mathrm{N_j}$ atoms of kind j at a distance $\mathrm{R_j}$. The back scattering equation from this atom is $\mathrm{t}\left(\mathrm{q}\right)$ and $\delta\left(\mathrm{q}\right)$ is the phase shift. Atomic vibrations are accounted by the Debye-Waller like factor exponential in σ and Λ is the mean free path. While analysing the absorption spectra usign Artemis software, $\mathrm{R_j}$

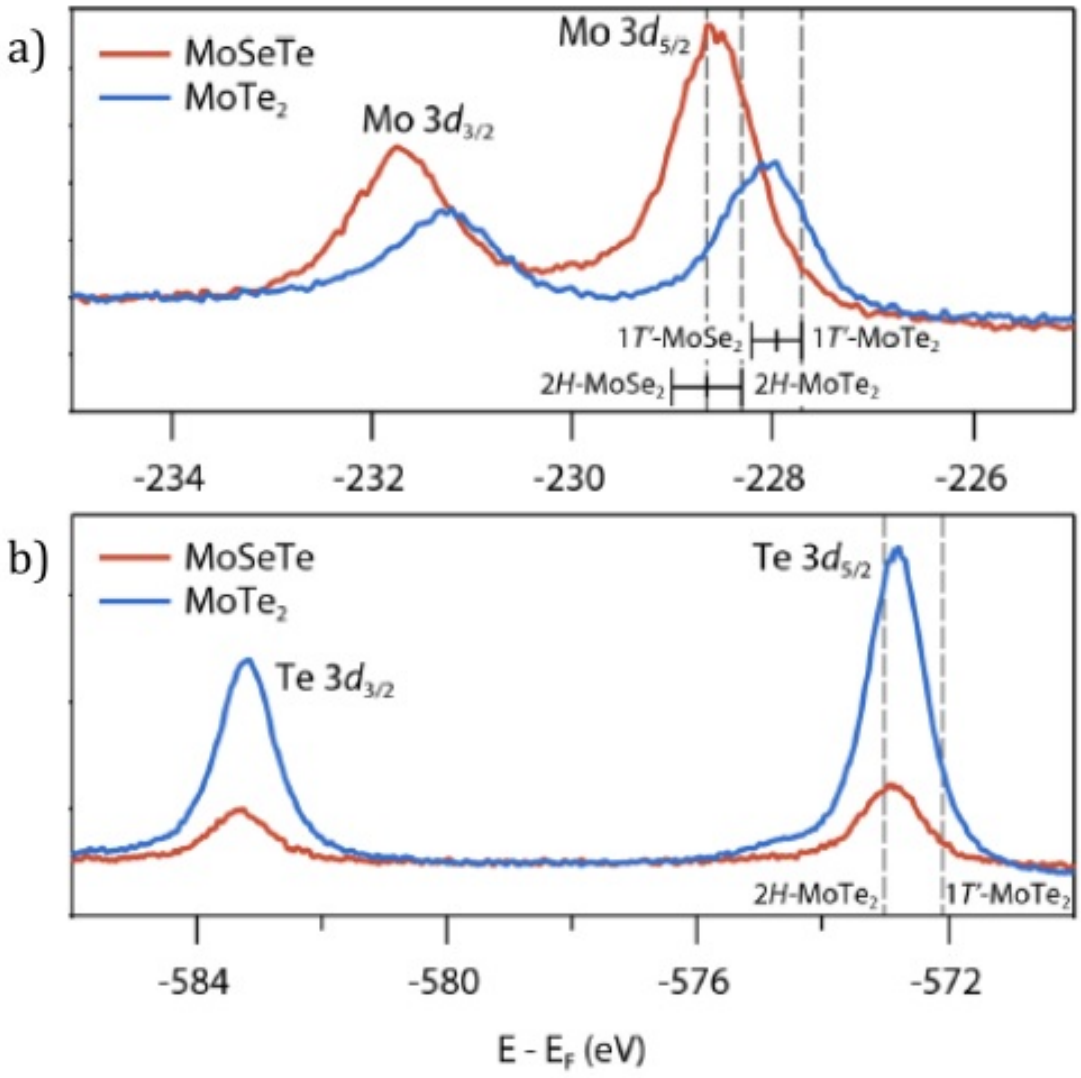

Figure 2.7: a) Mo-3d peaks from $MoSe_{2-x}Te_x$ have binding enregy between the values for 2H-$MoSe_2$ and 2H-$Mote_2$. (b) Te-3d peaks.

and σ are fitting parameters while $\mathrm{N_j}$ is set by the crystal structure. All absorption data were collected at the Se-K edge and calibrated using a Se foil.

The k, k^2 and k^3 weighted EXAFS oscillations are presented in Figure 2.8. The corresponding Fourier transforms were calculated for $\mathrm{k}-$ range of $3.00 - 11.98$ Å^{-1} and a hanning window from $1.5 - 8.0$ Å was used. Two peaks around

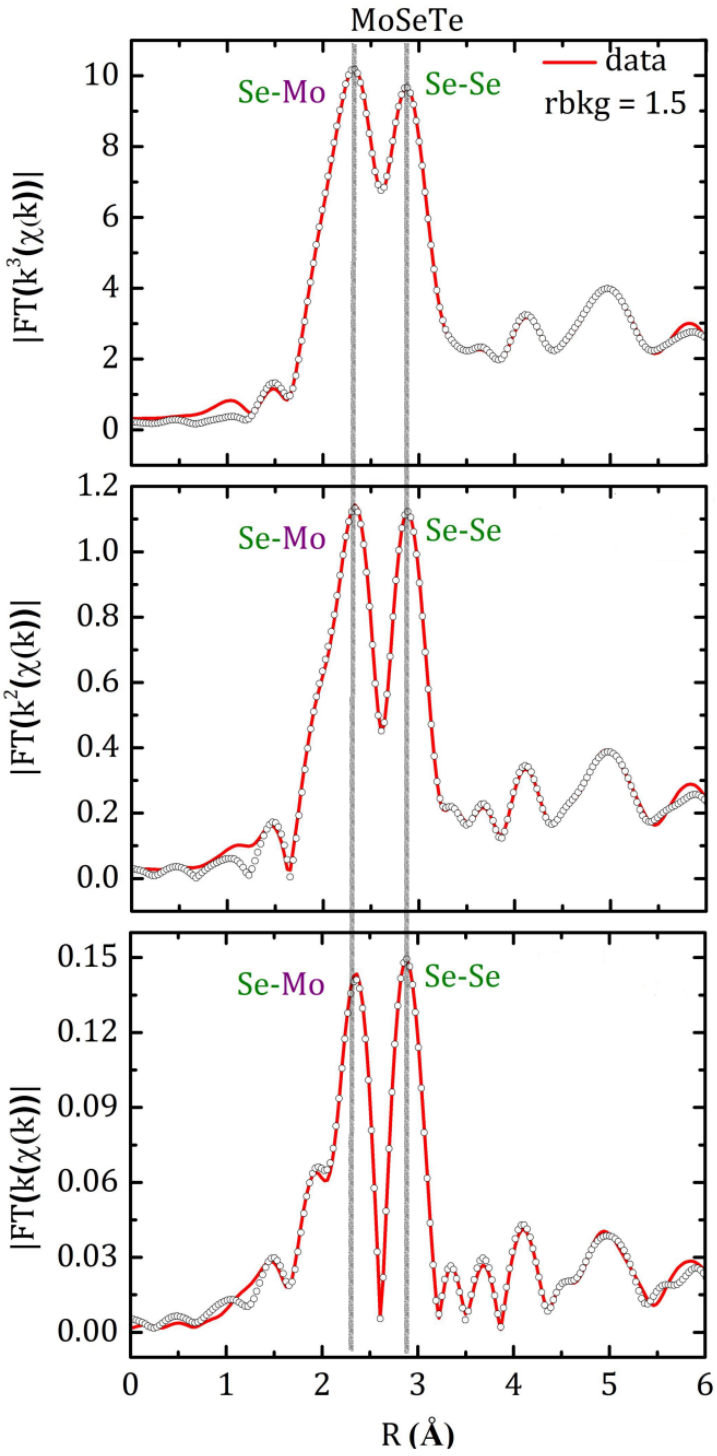

Figure 2.8: EXAFS data (red line) and fit (empty black circle) for $MoSe_{2-x}Te_x$ obtained at the Se K-edge. Plots are generated at different k-weights of (a) k=3, (b) k=2 and (c) k=1. The phase shifted peaks correspond to different bond lengths.

2.25 Å and 3.00 Å. These are attributed to Se-Mo and Se-Se bonds. They appear at radial distances shorted than actual bond lengths due to phase shifts accounted by $\delta_{\mathrm{j}}\,(\mathrm{q})$ in the EXAFS equation. The real space Fourier transforms of the oscillations were fit in Artemis 0.9.20 of the IFFEFIT package. During the fit, energy was kept constant. The fitting parameters were S_0^2 (same for all scattering paths), number of scatterers $\mathrm{N_j}$ and Debye-Waller factors σ_{j}^2. The maximum variable parameters allowed is given by $\left[\frac{2\Delta \mathrm{k}\Delta \mathrm{R}}{\pi}\right]$ where $[\mathrm{x}]$ is the greatest integer values less than x. All scattering paths considered to get the best fit are describes in the appendix A. The absorbing Se atom has 3 Mo neighbours in the first coordination shell as it is trigonally bonded. There are 6 Se atoms at a distance of 1 lattice spacing.

Scattering atom	$\mathrm{N_j}$	σ_{j}^2	$\mathrm{R_j}$ $\left(\text{Å}\right)$
Mo	3	0.004	2.51-2.53
Se	6	0.009	3.32-3.35

Table 2.6: Fit parameters for the Mo and Se nearest neighbour shells.

A Se-Se bond length of ~ 3.35 Å is seen to be the best fit to the measured oscillations. This bond length is actually the lattice parameter of the 2H-phase $MoSe_{2\text{-}x}Te_x$ alloy. $MoSe_2$ is reported to have an in-plane lattice constant of 3.25-3.33 measured by different techniques. This increase in lattice parameter is indicative of a chalcogen alloyed sample. The Se-Mo bond is measured by fitting the first peak in the EXAFS oscillations. The obtained value of ~ 2.55 Å is slightly larger than the Se-Mo bond length in unalloyed $MoSe_2$ (~ 2.5 Å). The lattice constant of ~ 3.32 Å obtained from LEED is in reasonable agreement with EXAFS results.

All the results obtained for this sample on GaAs confirm two key observations:

(i) The TMD film is chalcogen alloyed with a composition of $MoSe_{1.63}Te_{0.27}$ and (ii) It is grown in the 2H polytype.

2.4 Conclusion

We have been able to demonstrate the MBE growth of alloyed $MoSe_{2-x}Te_x$ films. It is shown that co-deposition of Se and Te at 400°C results in preferential Se incorporation and Te exclusion. However, pulsing the injection of Se and Te into the growth chamber at a lower temperature of 340°C results in growths with significant Te compositions. This is directly indicated by the shifted features in XRD, Raman, transient absorption and XPS spectra. The presence of Te is seen to promote the oxidation of Mo and Se. The impact of alloying on electronic properties are potentially interesting studies.

CHAPTER 3

Grazing incidence X-ray diffraction to study epitaxy of 2D materials

3.1 Literature

Another important area of materials research has been the integration of graphene and TMDs. Charge transport in layered films perpendicular to the layer is crucially dependent on the rotational alignment of these materials. Heteroepitaxy of 2D materials can also introduce strain in them, which can impact bandgaps and band alignments. While several researchers have identified strain by studying its effect on the absorption and emission spectra, direct mapping of strain in real or reciprocal space has not been much investigated. Atomic Force Microscopy (AFM) and Scanning Tunnelling Microscopy (STM) provide a direct means of imaging the grains and lattices in real space. The capability of this technique in studying alignments, Moire patterns and strain renders it as a very powerful tool. An indirect way of mapping strains is Raman spectroscopy. There is comprehensive literature on the connection between strain in graphene and shifts in the 2D and G phonon modes. Uniaxial and biaxial strain measurements on different flexible substrates (polyethylene terephthalate-PET, polymethyl methacrylate-PMMA) have shown the graphene G and 2D peaks to redshift with increasing tensile strain[48]. Density functional theory calculations on free-standing graphene agree with experimental results for strains $<$1%. The raman shift under uniaxial strain is largely attributed to strain and possibly to relative shift in the Dirac cone positions (since the D mode is an intervalley scattering process). Biaxial strains can be used to more accurately evaluate the D mode peak shift since the relative positions of the Dirac cones are

unchanged. Additionally, graphene embedded in PMMA cantilevers showed a polynomial variation of the 2D peak position with strain[1]. The 2D peak was reported to blueshift under compression. The highest frequency was measured at 0.6% compression beyond which it decreased polynomially. Redshifted G and 2D peaks in mono and tri-layer graphene under tensile strains ≤0.78% have been understood by considering bond length changes[49]. Weakening of the C-C bond due to elongation lowers the vibrational energies.

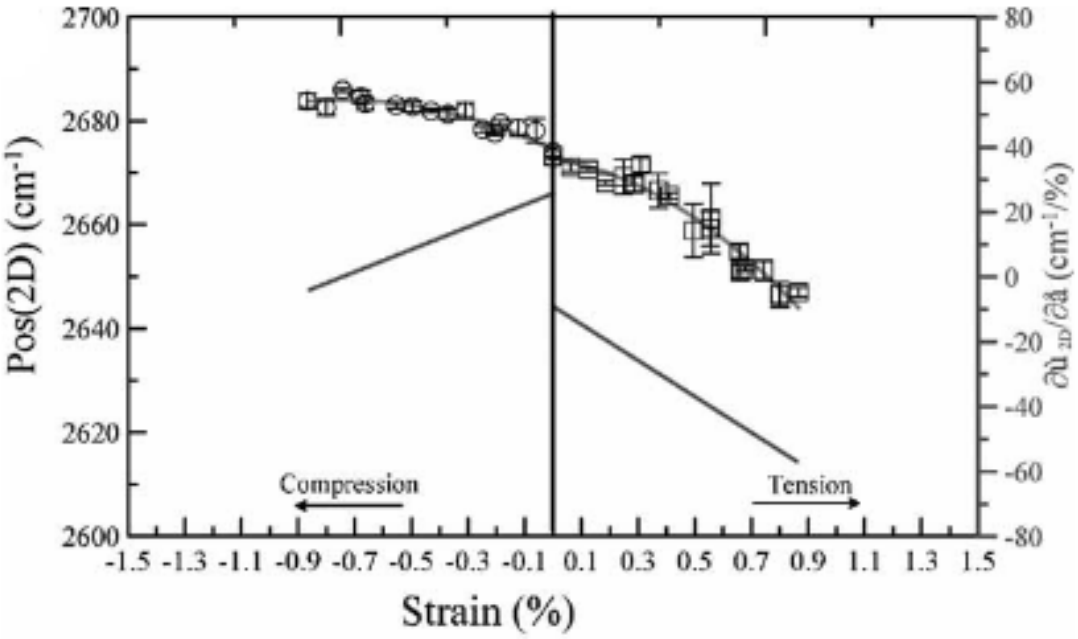

Figure 3.1: Polynomial curves of degree 2 were used to fit the frequency against both tensile and compressive strain[1].

Recently, CVD grown and exfoliated monolayer MoS_2 was biaxially strained by 5%, and the bandgap was found to reduce by ~ 500 meV[50]. The A_{1g} and E^1_{2g} Raman modes were observed to red shift for biaxial tensile strains up to 2.5%. Castellanos-Gomez et al. have studied the effect of up to 2.5% tensile strain on the phonon frequencies and bandgap of few layer MoS_2[51]. The in-plane E^1_{2g} mode was recorded to have a larger redshift than the out of plane A_{1g} mode.

The modification of the electronic band structure was observed in the photoluminescence spectra. The A and B exciton energies were redshifted on wrinkled MoS_2 as compared to the flat regions.

In this work, we present the use of synchrotron x-ray diffraction to comparatively study the MBE and CVD growth of chalcogenide films on SiC substrate. Grazing incidence X-ray diffraction (GI-XRD) is used to investigate key properties such as rotational alignment, strain and grain size in few nanometre thick films. Also, the surface sensitivity of this technique is used to study the effect of air exposure on GaSe.

3.2 Setup

The geometry of GI-XRD is described in this paragraph. The in-plane angle is ν and the out-of-plane angle is δ. Planar scans to check the symmetry of the samples are represented as ϕ scans (obtained at certain Bragg angles). Diffraction scans measured along $\nu - \phi$ (analogous to $\theta - 2\theta$) are plotted in reciprocal space. The incident angle η was set at 0.155°. The incident energy was set at 11.3 keV (1.097 $Å^{-1}$).

3.3 Chalcogenide films on epitaxial graphene on 6H-SiC(0001)

In this section, we discuss diffraction data from 5 samples. 2 films were grown by CVD (MoS_2 and WSe_2) and 3 films were grown by MBE ($MoSe_2$, $SnSe_2$ and Se capped $SnSe_2$ which is denoted as cap-$SnSe_2$).

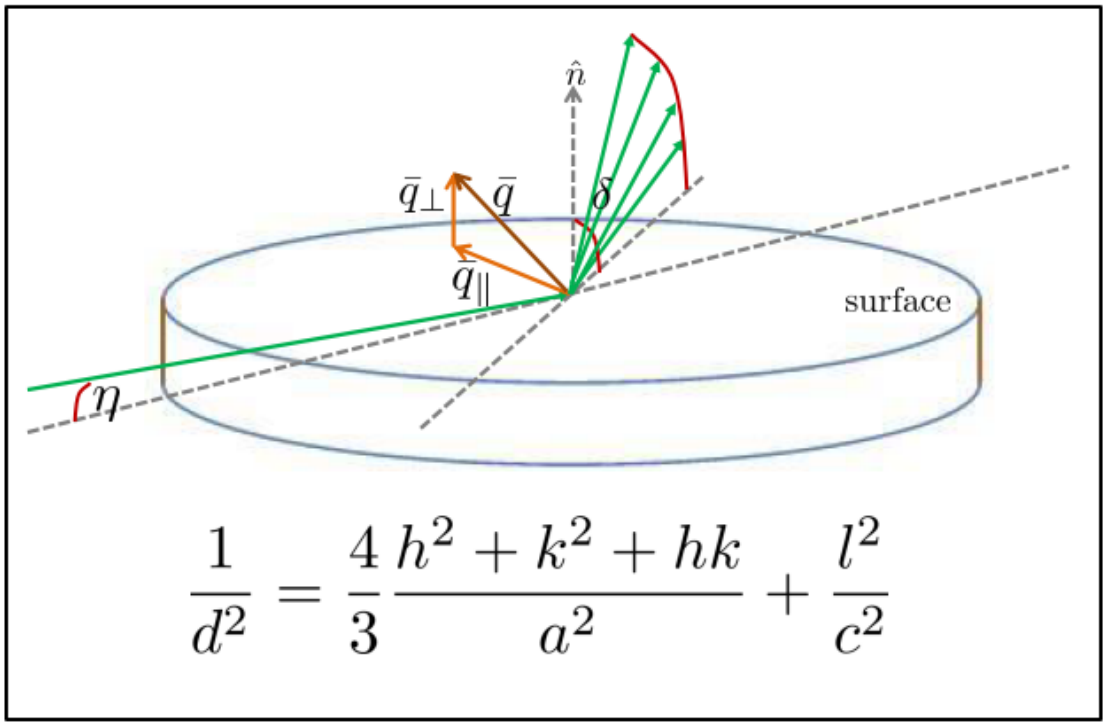

Figure 3.2: GI-XRD schematic and inter planar spacing d(hkl) for the hexagonal Bravais lattice with in plane lattice constant 'a' and out of plane lattice constant 'c'.

3.3.1 Registry of the films to the substrate

It is well known that epitaxial graphene and SiC have a 30° in plane misalignment[52, 2]. Since the chalcogenides, graphene and SiC all have hexagonal symmetry, the films are likely to be rotationally aligned to either graphene or SiC. ν-ϕ scans taken at 2 different ϕ angles rotated by 30° enable us to map the registry of the chalcogenide films. These results are depicted in Figure 3.3.

MBE films: From Figure 3.3-II (c) & (d), it can be seen that cap-$SnSe_2$ is rotationally commensurate with SiC. The graphene diffraction peak at ~3 $Å^{-1}$ appears when ϕ is rotated by 30°. The cap-$SnSe_2$ sample is seen to have many diffrac-

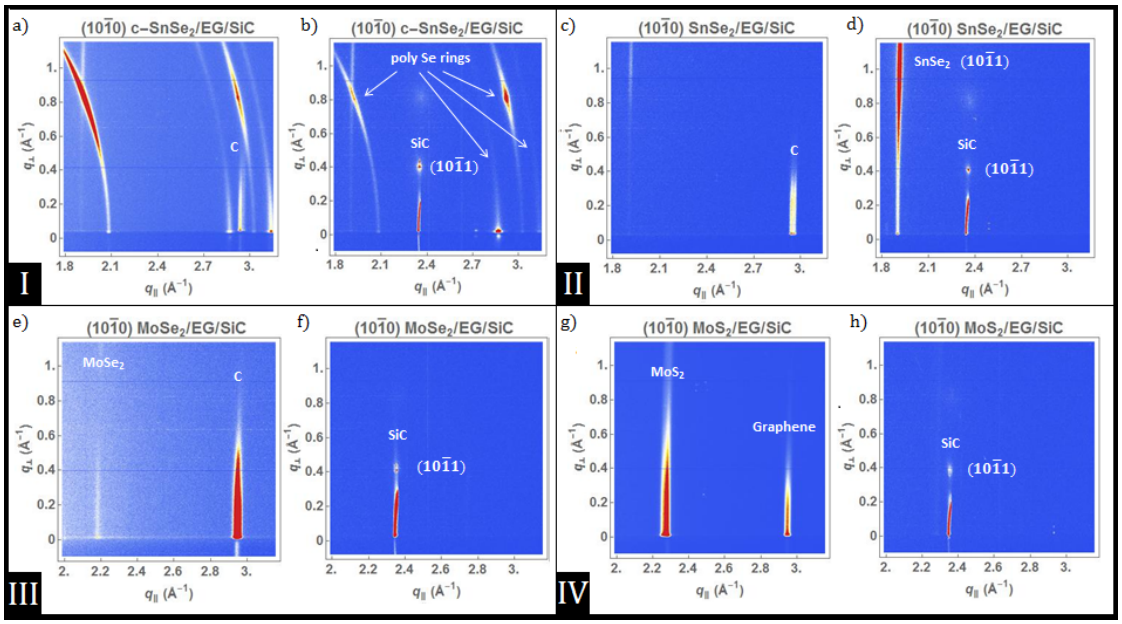

Figure 3.3: Images on the left and right side inside each box (I-IV) were obtained after rotating ϕ by 30°.

tion rings in the image which arise from the polycrystalline Se cap (Figure 3.3-I). $MoSe_2$ however is aligned to graphene, as seen in Figure 3.3-III. Preferential orientation of MBE grown $MoSe_2$ on graphene has been demonstrated from Low Energy Electron Diffraction[18, 3].

CVD films: The commensurate alignment of MoS_2 is identical to MBE $MoSe_2$. This is shown in Figure 3.3-IV. The alignment of CVD MoS_2 and graphene has been observed previously[2]. We report similar behavior for CVD WSe_2 on graphene, shown in appendix Figure B.1 . Rotational alignment of CVD WSe_2 is similar to that reported for MBE WSe_2 on graphene[4]. These details are summarised and tabulated in table 3.1.

It can also be observed from Figure 3.3 that the CVD graphene and SiC peaks appear at angular positions (ϕ) separated by 30°. This is in agreement with a pre-

Growth	Film ID	Alignment	
		Graphene	SiC
MBE	cap-$SnSe_2$	30° rotated	✓
	$SnSe_2$	30° rotated	✓
	$MoSe_2$	✓	30° rotated
CVD	WSe_2	✓	30° rotated
	MoS_2	✓	30° rotated

Table 3.1: MoS_2, $MoSe_2$ and WSe_2 are rotationally commensurate with graphene. $SnSe_2$ is 30° misaligned.

vious study[52] which showed the 30° rotation of graphene($11\bar{2}0$) & ($2\bar{1}\bar{1}0$) with respect to SiC($11\bar{2}0$) & ($2\bar{1}\bar{1}0$). This can however be contrasted with rotational alignment in graphene growth reported using gas-source MBE[53]. RHEED images obtained during gas-source MBE[53] growth of graphene (using cracked ethanol) do not show any lateral alignment. Instead, ring patterns were observed and attributed to graphene. Another article reported the appearance of diffraction peaks from these 2 materials at the same ϕ positions, confirming lateral alignment[5].

The nature of the $SnSe_2$ reflections in Figure 3.3-III and IV needs some discussion. It is noted that a strong peak at $q_\perp = 0$ is not seen for $SnSe_2$ in Figure 3.3-III. As we move along the $q_\perp$ axis, the intensity of the $SnSe_2$ ($q_\perp$ ~1.9 $Å^{-1}$) increases. This peak is due to diffraction from higher order planes where the Miller index $l \neq 0$. $SnSe_2$ has been widely known to crystallise in the CdI_2 structure, having the 1T polytype[54]. Recent articles have shown the growth of 1T phase $SnSe_2$ by MBE[55] and direct transport method[56]. Our observations indicate that the $SnSe_2$ is of 1T-polytype where the ($10\bar{1}0$) reflection is weaker. The intensity profiles of the films along the $q_\perp$ axis are discussed in subsection E.

3.3.2 Lattice constants of the chalcogenide films

The $(10\bar{1}0)$ reflections from the chalcogenide films are discussed in this section. All the diffraction peaks are plotted in figure 3.4 and the calculated and reported lattice constants along the a1 (& a2) crystal axes are listed in Table 3.2.

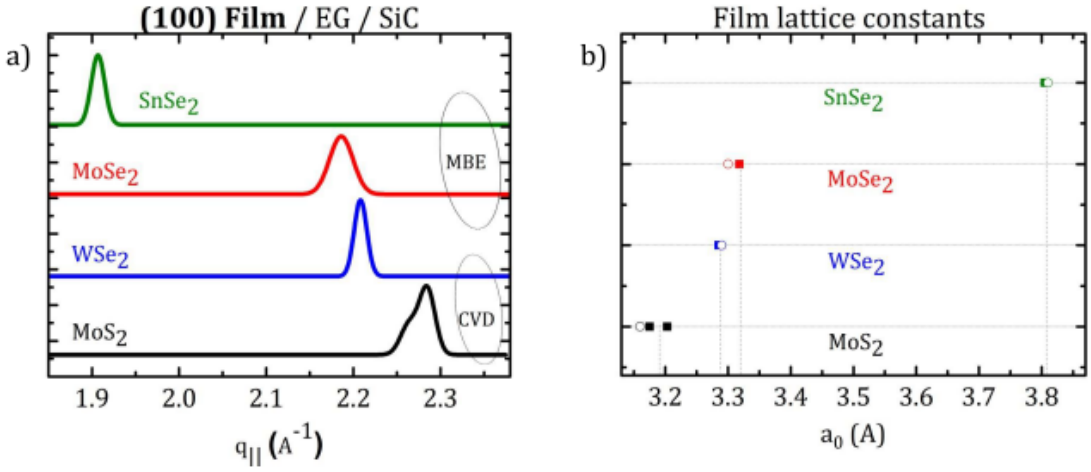

Figure 3.4: (a) $(10\bar{1}0)$ chalcogenide peaks and (b) calculated in-plane lattice constants. The solid squares and empty circles represent our calculations and reported lattice constant values respectively[2, 3, 4].

Growth	Film ID	Film $10\bar{1}0$ peak $Å^{-1}$		Lattice constant Å		Grain Size (nm)
		# 1	# 2	a_1	a_2	
MBE	$SnSe_2$	1.906		3.805		~80
	$MoSe_2$	2.186		3.318		~30
CVD	WSe_2	2.208		3.285		~80
	MoS_2	2.264	2.285	3.203	3.175	~50

Table 3.2: Lattice constants along the basal plane have been calculated by fiting the peaks in figure 3.4. The error in the calculated lattice constants is estimated to be 0.004 Å (considering energy resolution of the beam and fitting errors).

MBE films: We observe single peaks for $SnSe_2$ and $MoSe_2$. The in-plane lattice constants calculated from these $(10\bar{1}1)$ and $(10\bar{1}0)$ peaks bear excellent agreement with reported values[20, 57, 55, 58].

CVD films: WSe_2 is grown by MOCVD using gaseous precursors and exhibits a single sharp peak at the expected wave vector. The observed signal for MoS_2 can be deconvoluted into two peaks. The peak at $q_{||} = 2.285$ $^{-1}$ corresponds to a lattice constant of 3.17 , which is the known unstrained lattice parameter. The second peak at lower $q_{||}$ (or higher lattice) is originates from tensile strained MoS_2. This can be possible if certain substrate regions have multilayer coverage leading to strain relaxation and other regions have ML coverage (which is strained by the underlying graphene). Temperature gradients along the tube furnace (during MoS_2 growth) can plausibly result in non-uniform coverages.

Graphite is known to have a negative thermal expansion coefficient in the basal direction (α_a) at temperatures below 650 K[59, 60, 61, 62]. MoS_2 has a positive thermal expansion coefficient at all temperatures[63]. The lateral expansion of graphene during cooling from growth temperature to room temperature could induce strain in the lower MoS_2 layer. .

The crystallite sizes were calculated from the full width half maxima (FWHM) of the $(10\bar{1}0)$ reflections. Since the Miller indices k & l = 0 for $(10\bar{1}0)$ planes, it can be treated as a 1D chain of atoms. By expressing the Scherrer equation in reciprocal space[64], the grain size can be estimated as

$$s = \frac{2}{\sqrt{3}} * \frac{4\theta_o}{\Delta q}$$

where θ_o is obtained from the definition of FWHM for a 1D set of planes and Δq is the FWHM in $Å^{-1}$. It is however important to note that this only gives a lower bound to the crystallite size as the peak broadening can also be a result of other effects besides confinement.

3.3.3 Effect of growth conditions on bilayer graphene

Here we compare and discuss the nature of the graphene spetra for samples grown by MBE and CVD. In our previous work[18], we had observed a blue shift in the 2D Raman peak of graphene after MBE growth of sub ML $MoSe_2$ (on SiC(0001) substrate). By studying the lateral strain in graphene, we aim to understand that result. All graphene films are at least 2 layers thick (on top of the buffer layer).

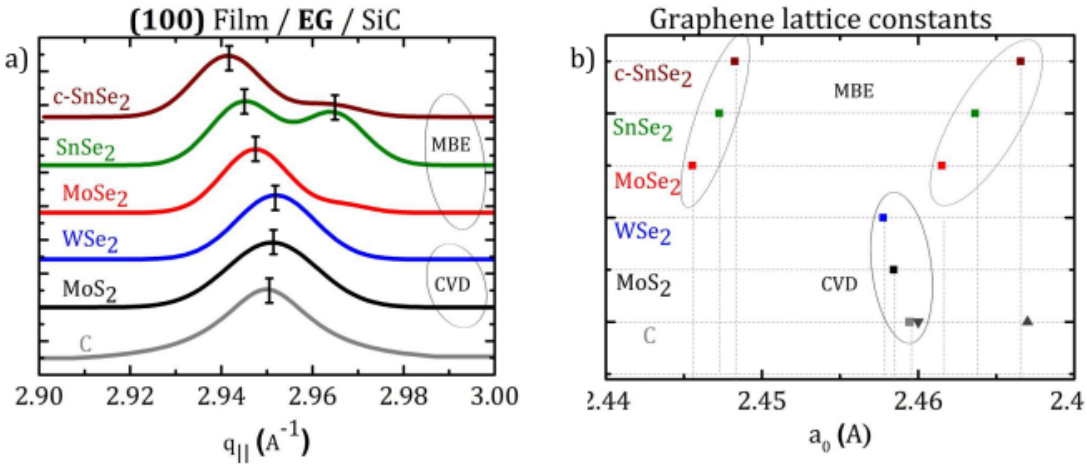

Figure 3.5: (a) Bilayer graphene peak positions. Doublet peaks observed in $MoSe_2$, $SnSe_2$ and cap-$SnSe_2$ while a single peak at an intermediate value is seen in MoS_2 and WSe_2. (b) Lattice constants calculated from peak positions are represented using filled squares. Filled triangles are references from a previous paper[5].

Growth	Film ID	Graphene $(10\bar{1}0)$ Å^{-1}		Lattice constant	
		Peak 1	Peak 2	a_1	a_2
MBE	cap-$SnSe_2$	2.941	2.963	2.466	2.448
	$SnSe_2$	2.945	2.964	2.463	2.447
	$MoSe_2$	2.947	2.966	2.461	2.445
CVD	WSe_2	2.952		2.457	
	MoS_2	2.951		2.458	
	Graphene	2.949		2.459	
Bulk	Graphite	-		2.461	

Table 3.3: The peak positions and in-plane lattice constants obtained from fitting the spectra in Figure 3.5 are listed here. The error in the calculated lattice constants is estimated to be 0.003 Å.

As depicted in Figure 3.5 (a), the graphene film on SiC without any chalcogenide growth (grey line) has a single peak corresponding to its relaxed lattice constant.

MBE films: The cap-$SnSe_2$, $SnSe_2$ and $MoSe_2$ films have 2 peaks at the graphene wave vector transfer. This indicates that the initially unstrained graphene is structurally separated into 2 layers. In all the MBE grown films, one set of peaks is observed very close to the bare graphene peak. The other set of peaks is seen at a higher parallel wave vector transfer ($q_{||}$). This suggests that some graphene layers are relaxed and some are compressively strained up to 0.65-0.7%. Blue shift of the 2D raman peak from these graphene samples is also indicative of compressive strain. Since the substrate is cooled uniformly, any strain induced in graphene is expected to be isotropic. Thus, the compression is more likely to be biaxial than uniaxial. This is important since uniaxial strains change the relative positions of Dirac cones in reciprocal space and might additionally impact the phonon frequencies. Biaxial strains preserve the relative positions of symmetry points and result in more accurate evaluations of peak shifts[48]. We note here that the Raman spectrum reported in our previous paper and lattice

constants reported here were measured for different samples which were grown under identical conditions.

CVD films: On the other hand, CVD grown MoS_2 and WSe_2 possess at the same angle as the bare graphene peak (blue, black and grey plots in Figure 3.5). Difference in cooling rates post growth can possible induce strain in the earlier samples.

3.3.4 Twinning and mosaicity of the chalcogenide grains

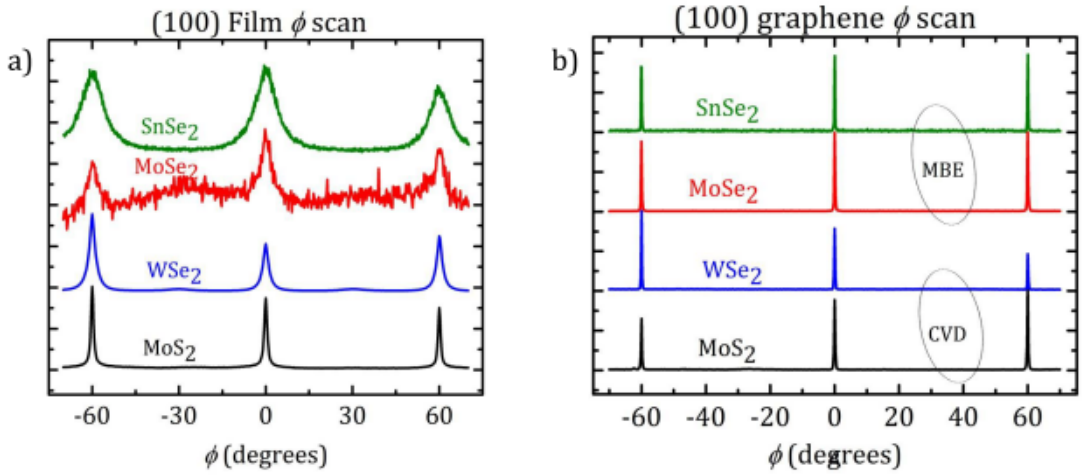

Figure 3.6: Planar ϕ scans show the rotational symmetry and relative mosaicity of all the films. (a) All chalcogenide films. (b) All graphene films. The diffraction signals from the chalcogenide/graphene films were isolated by setting the detector at the corresponding Bragg angle.

Angular ϕ scans over 140° were done at the $(10\bar{1}0)$ reflection to study the in-plane symmetry of all the films (Figure 3.6). As expected, we observed peaks separate by 60° which conforms the 6-fold symmetry of the films. The FWHM of these peaks can be used to infer the relative in-plane mosaicity of the films.

From Figure 3.6 (a), we observe that the MBE grown films ($SnSe_2$ and $MoSe_2$) have broader peaks the CVD grown films (MoS_2 and WSe_2). The FWHM (~4-9°) of MBE films is larger than the FWHM of CVD films (~1.2-2.4°). $MoSe_2$ and $SnSe_2$ have larger planar mosaicity than MoS_2 and WSe_2. Although the $SnSe_2$ peaks are broader, we do not observe a second set of peaks that might arise due to twinned grains. However, a small amount of twinning is observed in MoS_2 and WSe_2. A second set of 6-fold symmetric peaks appear 30° offset from the primary peaks. Graphene films grown on all substrates have identical peaks (Figure 3.6 (b)). The angular spread is measured to be much smaller with a FWHM of ~0.14-0.29°. The integration window was up to $\delta = 0.75°$ for these line scans.

3.3.5 Bragg rod profile

Figure 3.7 shows the integrated line profile of the Bragg rods. Bragg rod profiles from different polytypes of 7ML $NbSe_2$ have been compared in previous reports[64, 65]. $MoSe_2$ and WSe_2 do not show prominent higher order peaks indicating that the films are 1-2 ML. It is instructive to compare the profile of our MoS_2 film since there is a $(10\bar{1}3)$ peak at $q_\perp \sim 1.5$ Å. This can arise if there is significant surface coverage of few layer MoS_2. Such non-uniformity can explain the observation of 2 $(10\bar{1}0)$ peaks as discussed earlier. It is possible that the regions with 1ML MoS_2 are strained. Few ML growth can release this strain. The intensity profile of $SnSe_2$ shows the $(10\bar{1}1)$ peak, which is from the 1T phase. Microscope images from these samples are shown in the next section.

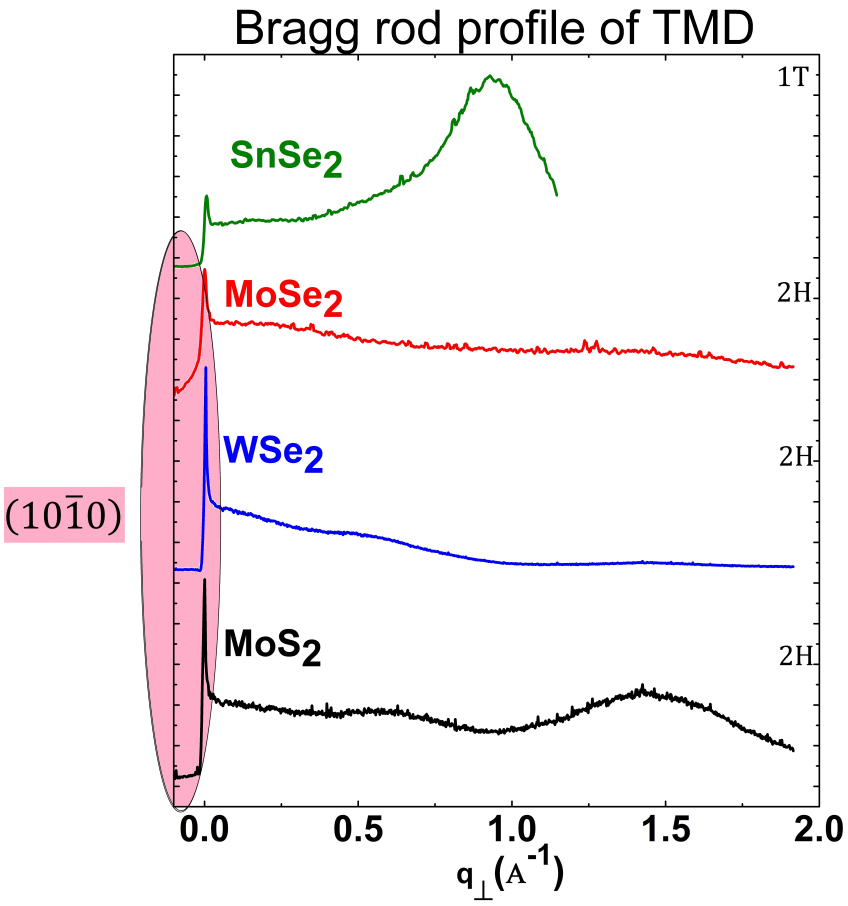

Figure 3.7: ~1ML $MoSe_2$ and WSe_2 have a flat bragg rod profile with no higher peaks. Few layer MoS_2 has a peak from the (10$\bar{1}$3) planes. The $SnSe_2$ peak is from (10$\bar{1}$1).

3.3.6 Microscopy images

The grain sizes obtained in the main text bear reasonable agreement with microscope images. Sharp (10$\bar{1}$1) peak seen in the Bragg rod profile arises from few layer $SnSe_2$. $MoSe_2$ does not show any higher order diffraction intensity after the strong (10$\bar{1}$0) at $q_\perp \sim 0$ as the film coverage is sub monolayer. There are no higher order Miller planes (index $l \neq 0$). WSe_2 profile shows low intensity

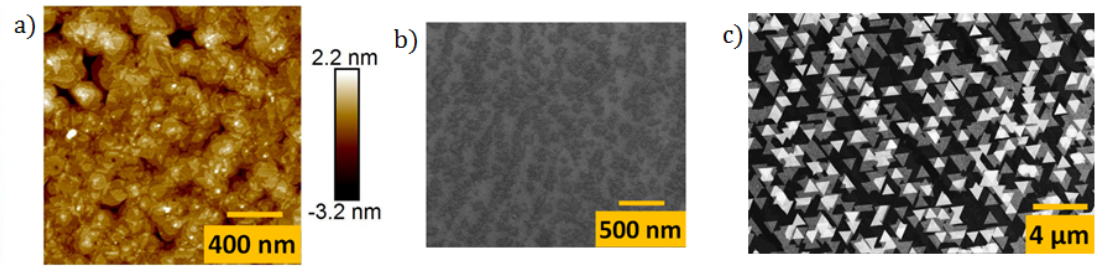

Figure 3.8: (a) AFM of $SnSe_2$ and SEM of (b) $MoSe_2$ and (c) WSe_2.

higher order peaks ($q_\perp \sim 0.5$ and 1.5 $Å^{-1}$) as the coverage is 1-2 ML.

3.4 Air sensitivity of GaSe on GaAs

We present the versatility and potential of this technique by investigating the effect of air exposure on MBE GaSe. Two sets of identical measurements were made on this sample with a gap of 8 hrs. We compare the diffraction intensities from the $(10\bar{1}0)$ peak in figure 3.9. Intensities are observed to reduce for both the ν and ϕ scans. The scans are indexed as '1st scan' and 'after air exposure' respectively. The two sets of measurements have the same baseline intensity which allow comparison of the peak properties. From (a), the integrated intensity is calculated to drop by ~45% after air exposure. ϕ scans in (b) show significant presence of twinned grains. From the Bragg rod profile in (c), the film is identified to be $\gamma - GaSe$ with calculated lattice constants of 3.756 (in-plane) and 23.882 (out of plane) listed in (d). These values agree well with literature [**?**]. The measured Raman spectra is also consistent with the γ phase. The reduction in GaSe $(10\bar{1}0)$ diffraction intensity was attributed to degradation of GaSe as the GaAs (112) substrate intensity profile was unchanged after air exposure (Figure 3.11).

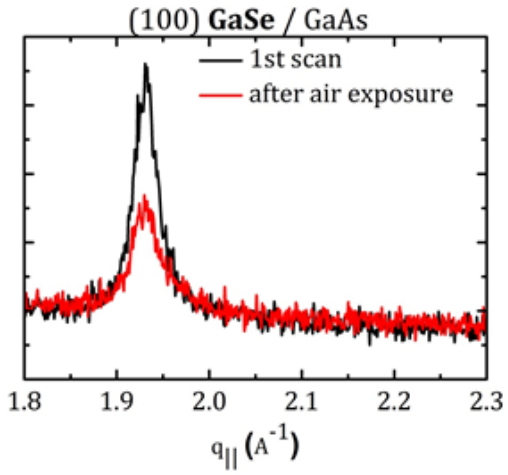

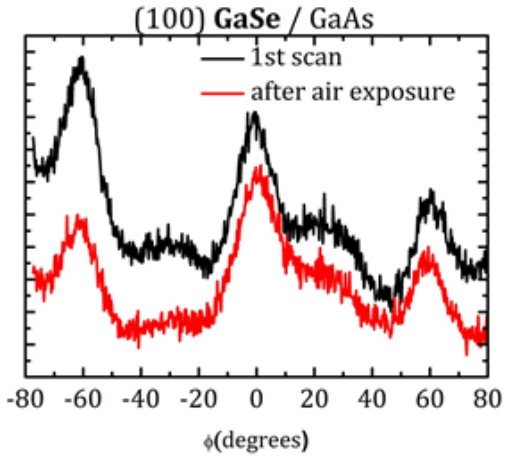

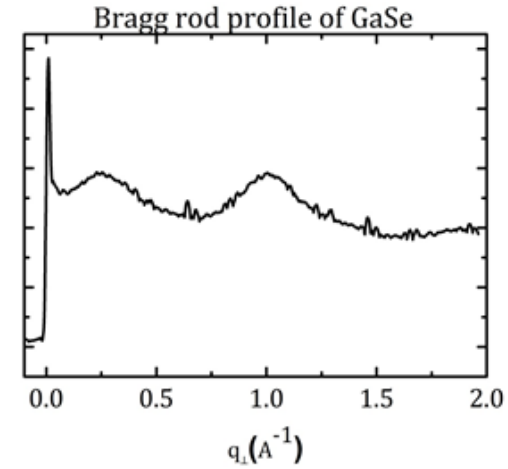

	Lattice constants	
∥	a (= b)	3.756 Å
⊥	c	23.882 Å

Figure 3.9: (a) GaSe(10$\bar{1}$0) peak from GaSe/GaAs. (b) ϕ scan shows extremely broad peaks (ϕ = -60°, 0° and 60°) as compared to the films grown on graphene. A weaker set of peaks appear in between the first set of peaks. The time interval between the two scans was 8 hrs.

3.5 Conclusion

We have shown the use of high brilliance X-ray sources to study van der Waals epitaxy in TMD materials. MoS_2, WSe_2 and $MoSe_2$ are shown to be rotationally aligned to graphene whereas $SnSe_2$ has a 30° misalignment. Graphene is shown to be compressively strained after MBE grown of TMD (above graphene) while CVD growths do not strain graphene. This is attributed to faster cooling rates

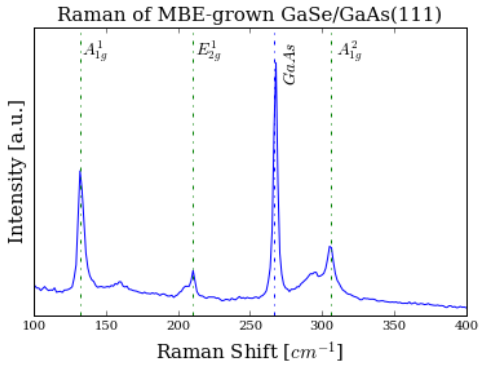

Figure 3.10: The raman spectrum of GaSe has A_{1g}^1, E_{2g}^1 and A_{1g}^2 peaks at the expected positions.

after MBE growth. CVD grown TMDs have larger grain sizes and lower mosaicity than MBE grown TMDs. Finally, air sensitivity in GaSe has been studied through diffraction measurements.

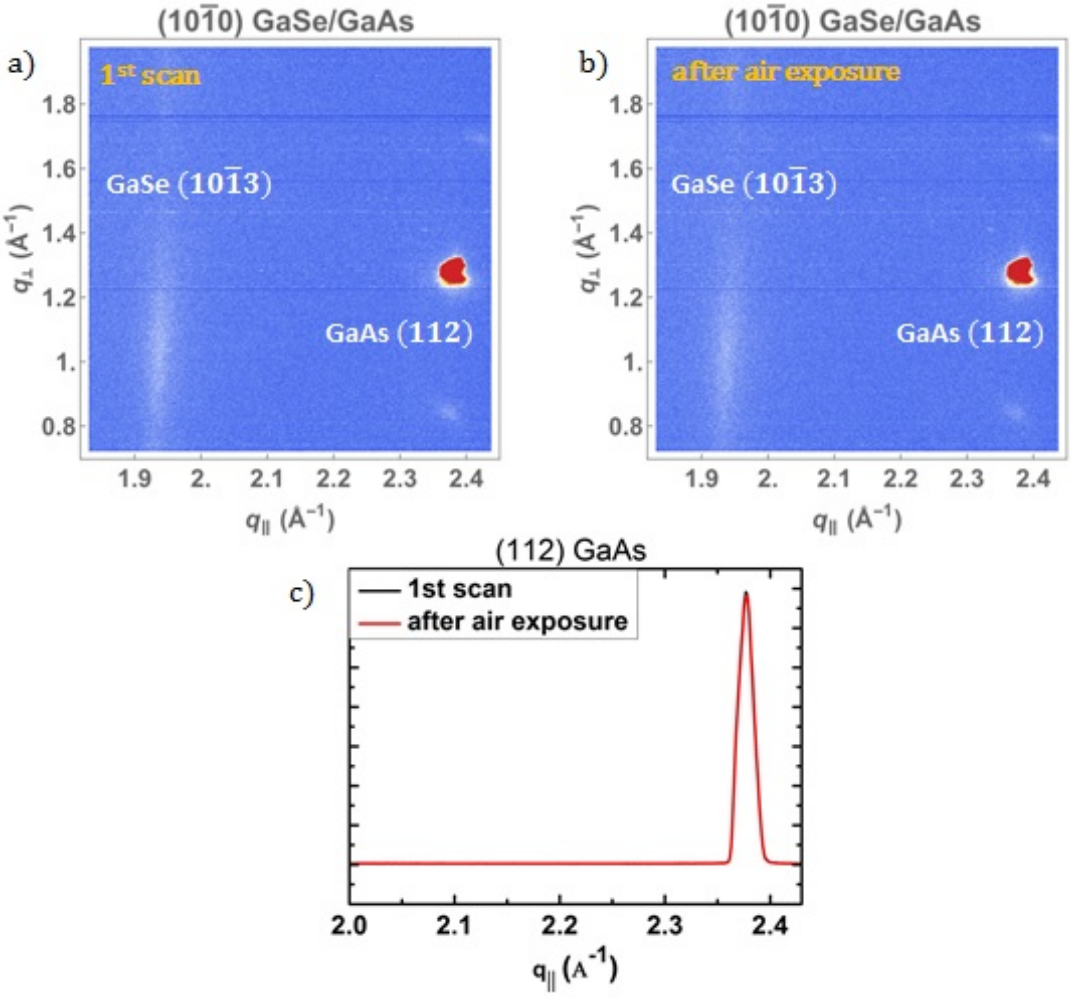

Figure 3.11: (a)- and (b)- 2D diffraction maps taken 8 hours apart show reduced intensity from the GaSe peak. (c) Line intensity profiles are identical across both the GaAs peaks.

APPENDIX A

$MoSe_{2-x}Te_x$ ALLOYS

A.1 Flux calculations

Se vapour is known to contain several oligomers[66]. The effective mass of the incident Se atoms is calculated by averaging with respect to the partial pressure of all oligomers in the vapour. This is described in equation A.1. Te atoms exist as dimers.

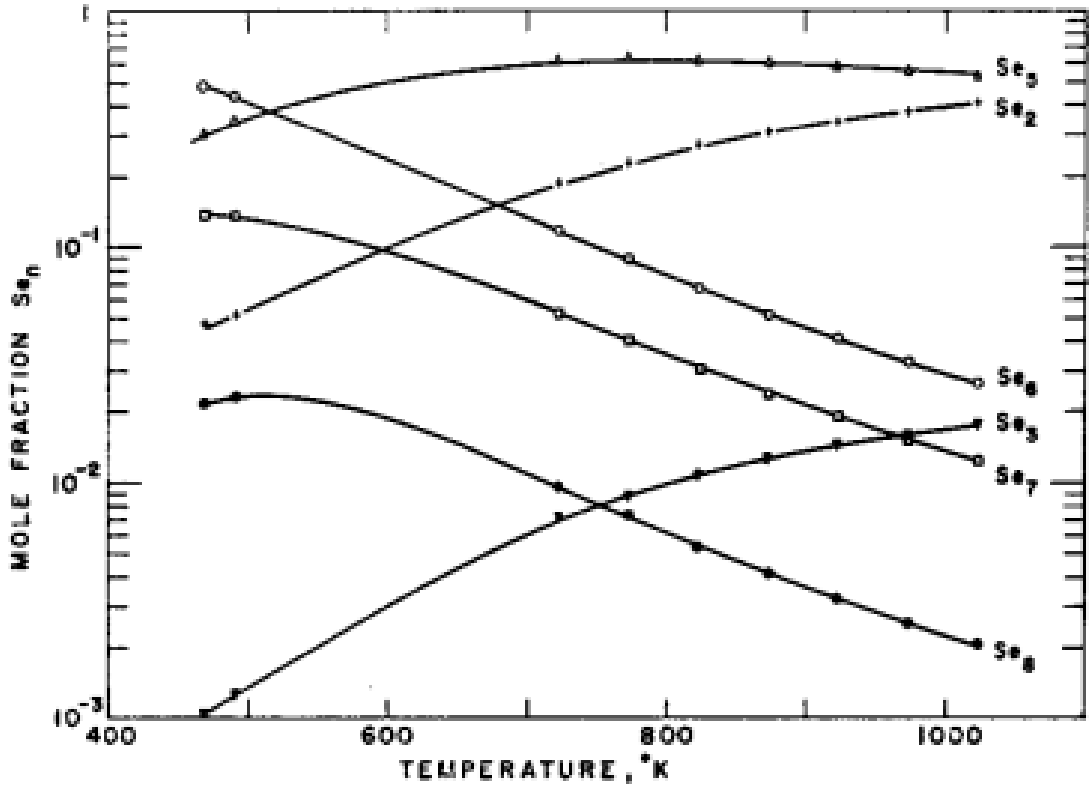

Figure A.1: Mole fraction of different oligomers in Se vapour as a function of temperature.

$$m_{Se} = \frac{\left(10^{-3} * 3m_{Se}\right) + \left(2x10^{-2} * 8m_{Se}\right) + \left(4x10^{-2} * 2m_{Se}\right) + \left(1.5x10^{-1} * 7m_{Se}\right) + \left(3x10^{-1} * 5m_{Se}\right) + \left(5x10^{-1} * 6m_{Se}\right)}{10^{-3} + 2x10^{-2} + 4x10^{-2} + 1.5x10^{-1} + 3x10^{-1} + 5x10^{-1}} \tag{A.1}$$

The flux of the impinging Se/Te atoms is related to the temperature (T), pressure (P) and mass (M) as

$$\phi = 3.513\,\mathrm{x}\,10^{22}\,\frac{\mathrm{P}}{\sqrt{\mathrm{MT}}}\ \mathrm{moles/cm^2-s} \tag{A.2}$$

A.2 Absorption spectrum and transitions

$MoSe_2$ and $MoTe_2$ have direct bandgaps at K, in the monolayer limit. Although few layer TMDs are known to have indirect bandgaps, their absorption spectrum is dominated by direct transitions occuring at K[51, 50]. The valence band is split due to spin-orbit coupling whereas. The neutral A and B excitonic transitions occur between the split valence bands and conduction band at K. The transition C happens close to Γ.

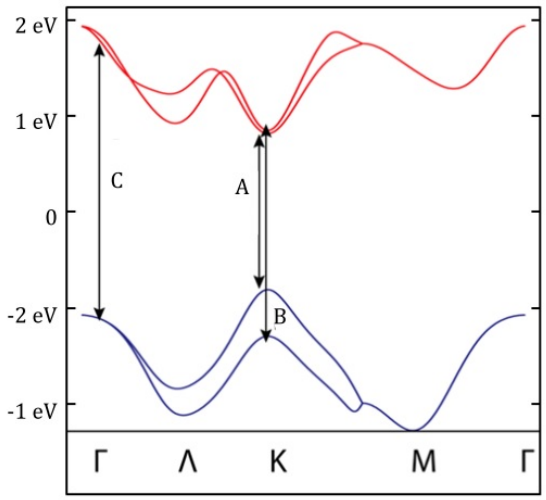

Figure A.2: Bulk $MoSe_2$ band diagram to depict the A, B and C excitonic transitions. Transitions A and B occur at the K point. Transition C is near the Γ point.

Measurements done on exfoliated few layer $MoSe_2$ and $MoTe_2$ have been compared with the films in series A and B in figure A.3.

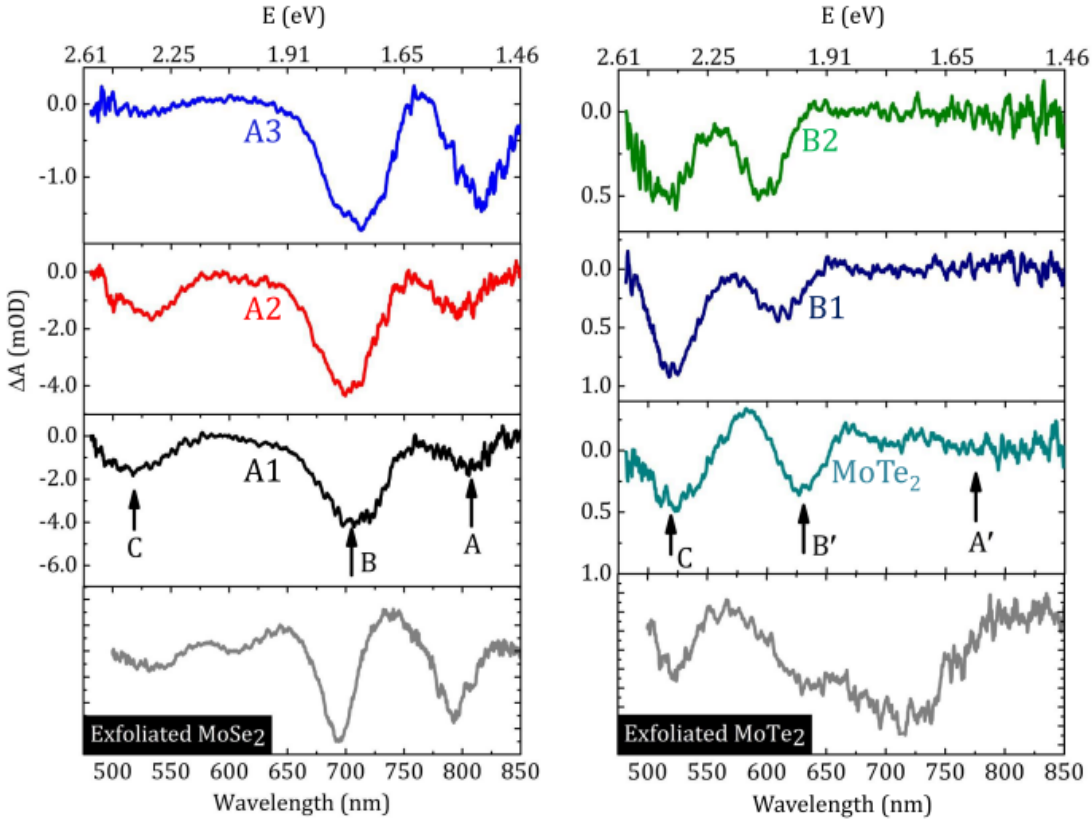

Figure A.3: TA spectra from bulk $MoSe_2$ and bulk $MoTe_2$.

A.3 XPS

All doublet energy separation values for data discussed in 2 were taken from the NIST XPS database. The C 1s peak at a B.E. of 284.5 eV was used as reference. In figure A.4, the survey scans for one sample in series A and B are shown. All major peaks are assigned to elemental core energies and Auger transition energies.

Figure A.5 shows the doublet components for Mo-3d, Se-3d and Te-3d peaks from $MoSe_{2-x}Te_x$. There are no oxidation peaks observed since the measurement was done in situ after decapping the Se cap. The solid grey line is the total fit peaks (using CasaXPS) and the experimental measurement is shown in black

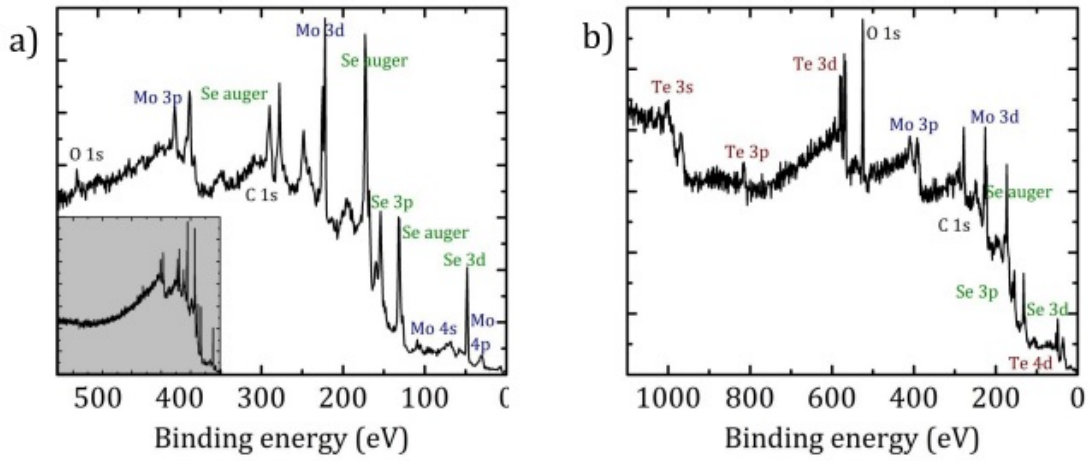

Figure A.4: (a) XPS survey scan for sample A1 ($MoSe_2$). (c) XPS survey scan for sample B2 ($MoSe_{2-x}Te_x$ 1:1).

circles.

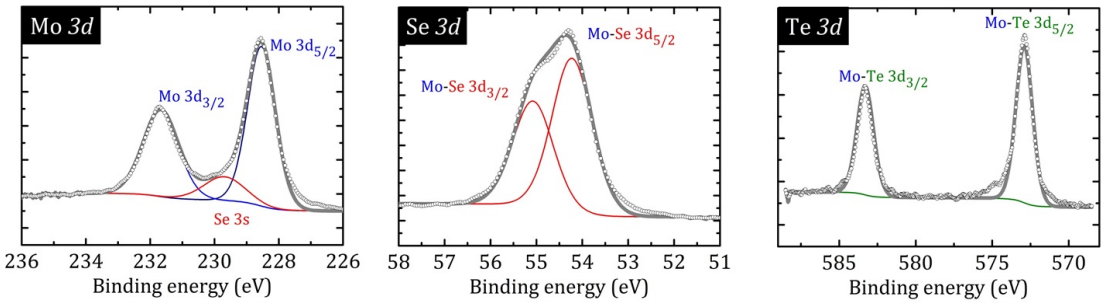

Figure A.5: (a) Mo-3d, (b) Se 3d and (c) Te-3d doublet peaks for the samples grown on GaAs have no oxide signals as the samples was decapped and measured in situ.

A.4 EXAFS

X-ray absorption data were obtained in the F3 beamline of the Cornell High Energy Synchrotron Source (CHESS).

A.4.1 Data acquisition

All spectra were obtained at the Se K-edge in the fluorescence mode. Transmission mode EXAFS data from a Se foil was used as reference. The pre-edge, edge and post-edge energy ranges and spacing are listed in table A.1. A total of 3 scans were taken.

Region	Lower limit	Upper limit	spacing	time
Pre-edge	-0.2 keV	-0.02 keV	0.005 keV	10 sec
Edge	-0.02 keV	0.05 keV	0.001 keV	10 sec
Post-edge	0.05 keV	0.747 keV (14 $Å^{-1}$)	0.05 $Å^{-1}$	10 sec

Table A.1: Energy regions and spacings to acquire X-ray absorption data.

A.4.2 Data processing and analysis

Athena 0.9.26 was used for standard pre-processing procedures. The scans were calibrated to the Se K-edge, aligned and merged prior to background subtraction. Subtraction of the pre-edge and normalisation of the data was done by defining linear and quadratic functions for the pre- and post-edge regions respectively. The images in figure A.6 were generated by using a hanning window from $1.0 - 8.0$ Å. As a result, there is relative more mismatch between the data and the fit at lower radial distances.

k^3- weighted plots obtained using different 'rbkg' parameters are compared in figure A.7. A clear difference is noticed at smaller R. There is better agreement between experimental and theoretical data when a larger 'rbkg' parameter is used. This is because 'rbkg' is the value below which all Fourier components are removed.

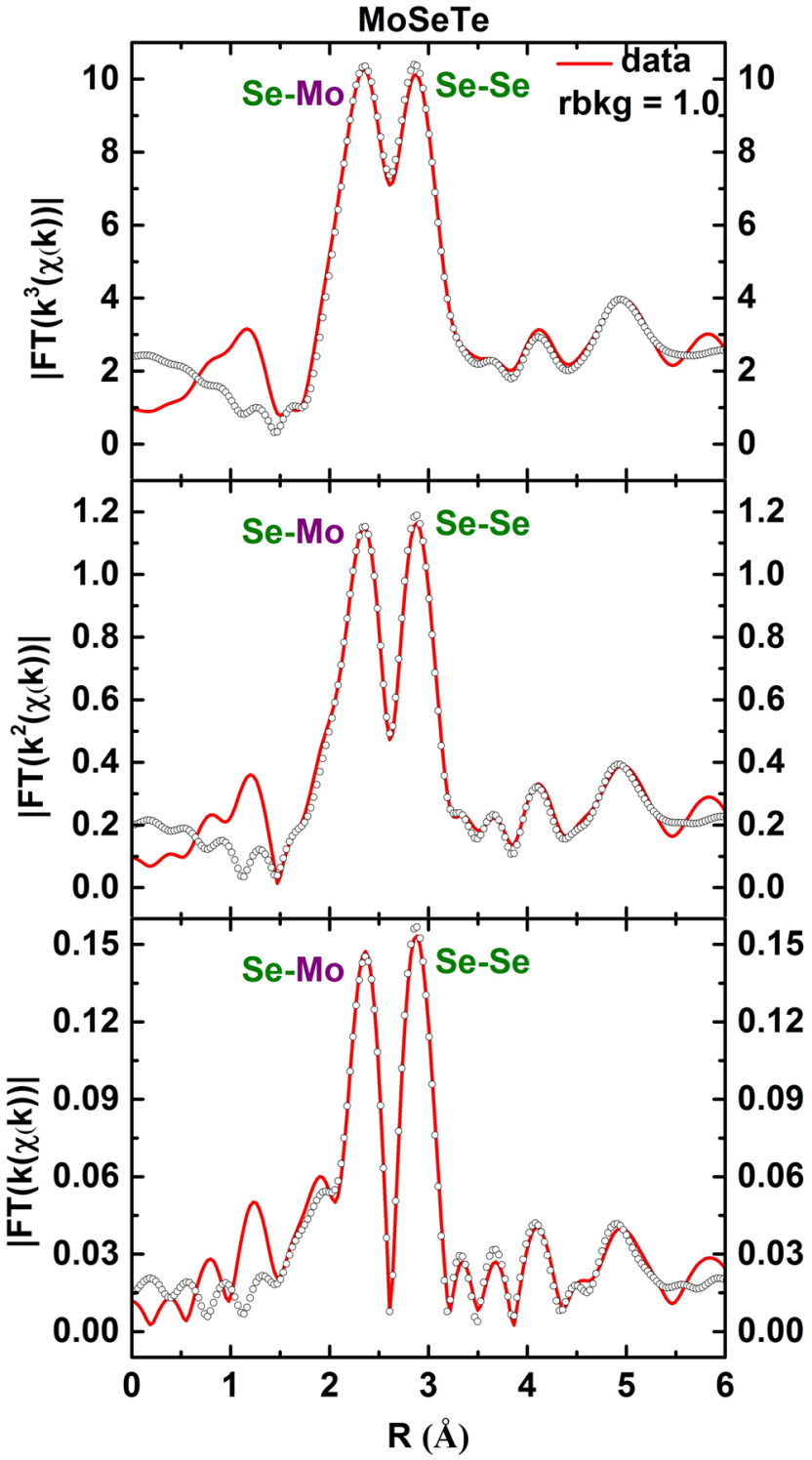

Figure A.6: EXAFS data (red line) and fit (empty black circle) for $MoSe_{2-x}Te_x$ obtained at the Se K-edge. Plots are generated at different k-weights of (a) k=3, (b) k=2 and (c) k=1. The phase shifted peaks correspond to different bond lengths.

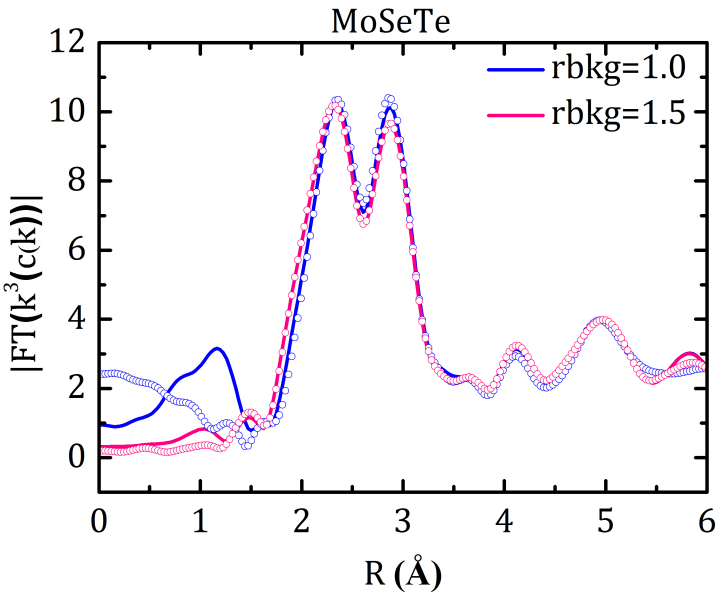

Figure A.7: EXAFS data (red line) and fit (empty black circle) for $MoSe_{2-x}Te_x$ obtained at the Se K-edge. Plots are generated at different k-weights of (a) k=3, (b) k=2 and (c) k=1. The phase shifted peaks correspond to different bond lengths.

APPENDIX B

GI-XRD

B.1 WSe_2 peak and alignment

Diffraction peaks from MoS_2, $MoSe_2$, $SnSe_2$ and cap-$SnSe_2$ obtained at different δ values were discussed in the main text. Figure B.1 shows the peaks from the WSe_2 sample. The alignment observed is similar to that seen in MoS_2 and $MoSe_2$.

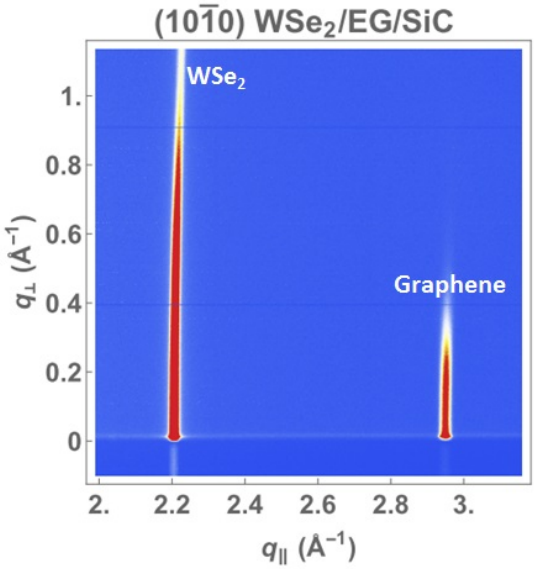

Figure B.1: The (10$\bar{1}$0) from WSe_2 is rotationally aligned with (10$\bar{1}$0) graphene.

BIBLIOGRAPHY

[1] Konstantinos Papagelis Rashid Jalil Andrea C. Ferrari Andre K. Geim Kostya S. Novoselov Georgia Tsoukleri, John Parthenios and Costas Galiotis. Subjecting a graphene monolayer to tension and compression. *small*, (5):2397, 2009.

[2] Xiaolong Liu, Itamar Balla, Hadallia Bergeron, Gavin P Campbell, Michael J Bedzyk, and Mark C Hersam. Rotationally commensurate growth of mos2 on epitaxial graphene. *ACS nano*, 10(1):1067–1075, 2015.

[3] Miguel M Ugeda, Aaron J Bradley, Su-Fei Shi, H Felipe, Yi Zhang, Diana Y Qiu, Wei Ruan, Sung-Kwan Mo, Zahid Hussain, Zhi-Xun Shen, et al. Giant bandgap renormalization and excitonic effects in a monolayer transition metal dichalcogenide semiconductor. *Nature materials*, 13(12):1091–1095, 2014.

[4] Jun Hong Park, Suresh Vishwanath, Xinyu Liu, Huawei Zhou, Sarah M Eichfeld, Susan K Fullerton-Shirey, Joshua A Robinson, Randall M Feenstra, Jacek Furdyna, Debdeep Jena, et al. Scanning tunneling microscopy and spectroscopy of air exposure effects on molecular beam epitaxy grown wse2 monolayers and bilayers. *ACS nano*, 10(4):4258–4267, 2016.

[5] T Schumann, M Dubslaff, MH Oliveira Jr, M Hanke, F Fromm, T Seyller, Lydia Nemec, Volker Blum, Matthias Scheffler, J Marcelo J Lopes, et al. Structural investigation of nanocrystalline graphene grown on (6 3× 6 3) r30-reconstructed sic surfaces by molecular beam epitaxy. *New Journal of Physics*, 15(12):123034, 2013.

[6] S. Horzum, H. Sahin, S. Cahangirov, P. Cudazzo, A. Rubio, T. Serin, and F. M. Peeters. Phonon softening and direct to indirect band gap crossover in strained single-layer mose$_2$. *Phys. Rev. B*, 87:125415, Mar 2013.

[7] Tingting Shen, Ashish V. Penumatcha, and Joerg Appenzeller. Strain engineering for transition metal dichalcogenides based field effect transistors. *ACS Nano*, 10(4):4712–4718, 2016. PMID: 27043387.

[8] Yi Zhang, Tay-Rong Chang, Bo Zhou, Yong-Tao Cui, Hao Yan, Zhongkai Liu, Felix Schmitt, James Lee, Rob Moore, Yulin Chen, et al. Direct observation of the transition from indirect to direct bandgap in atomically thin epitaxial mose2. *Nature nanotechnology*, 9(2):111–115, 2014.

[9] Aaron M Jones, Hongyi Yu, Nirmal J Ghimire, Sanfeng Wu, Grant Aivazian, Jason S Ross, Bo Zhao, Jiaqiang Yan, David G Mandrus, Di Xiao, et al. Optical generation of excitonic valley coherence in monolayer wse2. *Nature nanotechnology*, 8(9):634–638, 2013.

[10] Dong Hoon Keum, Suyeon Cho, Jung Ho Kim, Duk-Hyun Choe, Ha-Jun Sung, Min Kan, Haeyong Kang, Jae-Yeol Hwang, Sung Wng Kim, Heejun Yang, et al. Bandgap opening in few-layered monoclinic mote2. *Nature Physics*, 11(6):482–486, 2015.

[11] Jinglei Chen, Guanyong Wang, Yanan Tang, Jinpeng Xu, Xianqi Dai, Jinfeng Jia, Wingkin Ho, and Maohai Xie. Growth, stabilization and conversion of semi-metallic and semiconducting phases of mote2 monolayer by molecular-beam epitaxy. *arXiv preprint arXiv:1612.06105*, 2016.

[12] Ignacio Gutiérrez Lezama, Ashish Arora, Alberto Ubaldini, Céline Barreteau, Enrico Giannini, Marek Potemski, and Alberto F Morpurgo. Indirect-to-direct band gap crossover in few-layer mote2. *Nano letters*, 15(4):2336–2342, 2015.

[13] Cheng Gong, Hengji Zhang, Weihua Wang, Luigi Colombo, Robert M Wallace, and Kyeongjae Cho. Band alignment of two-dimensional transition metal dichalcogenides: Application in tunnel field effect transistors. *Applied Physics Letters*, 103(5):053513, 2013.

[14] R Schlaf, O Lang, C Pettenkofer, and W Jaegermann. Band lineup of layered semiconductor heterointerfaces prepared by van der waals epitaxy: Charge transfer correction term for the electron affinity rule. *Journal of applied physics*, 85(5):2732–2753, 1999.

[15] Rusen Yan, Sara Fathipour, Yimo Han, Bo Song, Shudong Xiao, Mingda Li, Nan Ma, Vladimir Protasenko, David A Muller, Debdeep Jena, et al. Esaki diodes in van der waals heterojunctions with broken-gap energy band alignment. *Nano letters*, 15(9):5791–5798, 2015.

[16] Mingda Li, David Esseni, Gregory Snider, Debdeep Jena, and Huili Grace Xing. Single particle transport in two-dimensional heterojunction interlayer tunneling field effect transistor. *Journal of Applied Physics*, 115(7):074508, 2014.

[17] Atsushi Koma, Koichiro Saiki, and Yasuhiro Sato. Heteroepitaxy of a two-dimensional material on a three-dimensional material. *Applied surface science*, 41:451–456, 1990.

[18] Suresh Vishwanath, Xinyu Liu, Sergei Rouvimov, Patrick C Mende, Angelica Azcatl, Stephen McDonnell, Robert M Wallace, Randall M Feenstra, Jacek K Furdyna, Debdeep Jena, et al. Comprehensive structural and optical characterization of mbe grown mose2 on graphite, caf2 and graphene. *2D Materials*, 2(2):024007, 2015.

[19] Hongjun Liu, Lu Jiao, Fang Yang, Yuan Cai, Xianxin Wu, Wingkin Ho, Chunlei Gao, Jinfeng Jia, Ning Wang, Heng Fan, et al. Dense network of one-dimensional midgap metallic modes in monolayer mose 2 and their spatial undulations. *Physical review letters*, 113(6):066105, 2014.

[20] Anupam Roy, Hema CP Movva, Biswarup Satpati, Kyounghwan Kim, Rik Dey, Amritesh Rai, Tanmoy Pramanik, Samaresh Guchhait, Emanuel Tutuc, and Sanjay K Banerjee. Structural and electrical properties of mote2 and mose2 grown by molecular beam epitaxy. *ACS applied materials & interfaces*, 8(11):7396–7402, 2016.

[21] E Xenogiannopoulou, P Tsipas, KE Aretouli, D Tsoutsou, SA Giamini, C Bazioti, GP Dimitrakopulos, Ph Komninou, Steven Brems, Cedric Huyghebaert, et al. High-quality, large-area mose 2 and mose 2/bi 2 se 3 heterostructures on aln (0001)/si (111) substrates by molecular beam epitaxy. *Nanoscale*, 7(17):7896–7905, 2015.

[22] Qiang Zhang, Yuxuan Chen, Chendong Zhang, Chi-Ruei Pan, Mei-Yin Chou, Changgan Zeng, and Chih-Kang Shih. Bandgap renormalization and work function tuning in mose2/hbn/ru (0001) heterostructures. *Nature Communications*, 7, 2016.

[23] Horacio Coy Diaz, Redhouane Chaghi, Yujing Ma, and Matthias Batzill. Molecular beam epitaxy of the van der waals heterostructure mote2 on mos2: Phase, thermal, and chemical stability. *2D Materials*, 2(4):044010, 2015.

[24] Suresh Vishwanath, Xinyu Liu, Sergei Rouvimov, Leonardo Basile, Ning Lu, Angelica Azcatl, Katrina Magno, Robert M Wallace, Moon Kim, Juan-Carlos Idrobo, et al. Controllable growth of layered selenide and telluride heterostructures and superlattices using molecular beam epitaxy. *Journal of Materials Research*, 31(07):900–910, 2016.

[25] Mei Zhang, Juanxia Wu, Yiming Zhu, Dumitru O Dumcenco, Jinhua Hong, Nannan Mao, Shibin Deng, Yanfeng Chen, Yanlian Yang, Chuanhong Jin, et al. Two-dimensional molybdenum tungsten diselenide alloys: pho-

toluminescence, raman scattering, and electrical transport. *ACS nano*, 8(7):7130–7137, 2014.

[26] Yanfeng Chen, Dumitru O Dumcenco, Yiming Zhu, Xin Zhang, Nannan Mao, Qingliang Feng, Mei Zhang, Jin Zhang, Ping-Heng Tan, Ying-Sheng Huang, et al. Composition-dependent raman modes of mo1- xwxs2 monolayer alloys. *Nanoscale*, 6(5):2833–2839, 2014.

[27] Sheng-Han Su, Yu-Te Hsu, Yung-Huang Chang, Ming-Hui Chiu, Chang-Lung Hsu, Wei-Ting Hsu, Wen-Hao Chang, Hau He Jr, and Lain-Jong Li. Band gap-tunable molybdenum sulfide selenide monolayer alloy. *Small*, 10(13):2589–2594, 2014.

[28] Horacio Coy Diaz, Yujing Ma, Sadhu Kolekar, José Avila, Chaoyu Chen, Maria C Asensio, and Matthias Batzill. Substrate dependent electronic structure variations of van der waals heterostructures of mose2 or mose2 (1- x) te2x grown by van der waals epitaxy. *2D Materials*, 4(2):025094, 2017.

[29] Lin Zhou, Kai Xu, Ahmad Zubair, Albert D Liao, Wenjing Fang, Fangping Ouyang, Yi-Hsien Lee, Keiji Ueno, Riichiro Saito, Tomas Palacios, et al. Large-area synthesis of high-quality uniform few-layer mote2. *Journal of the American Chemical Society*, 137(37):11892–11895, 2015.

[30] Thomas Anthony Empante, Yao Zhou, Velveth Klee, Ariana Elaine Nguyen, I-Hsi Lu, Michael D Valentin, Sepedeh A Naghibi Alvillar, Edwin Preciado, Adam J Berges, Cindy S Merida, et al. Chemical vapor deposition growth of few layer mote2 in the 2h, 1tand 1t phases: Tunable properties of mote2 films. *ACS nano*, 2017.

[31] Andrea Splendiani, Liang Sun, Yuanbo Zhang, Tianshu Li, Jonghwan Kim, Chi-Yung Chim, Giulia Galli, and Feng Wang. Emerging photoluminescence in monolayer mos2. *Nano letters*, 10(4):1271–1275, 2010.

[32] Ayse Berkdemir, Humberto R Gutiérrez, Andrés R Botello-Méndez, Néstor Perea-López, Ana Laura Elías, Chen-Ing Chia, Bei Wang, Vincent H Crespi, Florentino López-Urías, Jean-Christophe Charlier, et al. Identification of individual and few layers of ws2 using raman spectroscopy. *Scientific reports*, 3, 2013.

[33] H Terrones, E Del Corro, S Feng, JM Poumirol, D Rhodes, D Smirnov, NR Pradhan, Z Lin, MAT Nguyen, AL Elias, et al. New first order raman-active modes in few layered transition metal dichalcogenides. *Scientific reports*, 4:4215, 2014.

[34] Chendong Zhang, Yuxuan Chen, Amber Johnson, Ming-Yang Li, Lain-Jong Li, Patrick C Mende, Randall M Feenstra, and Chih-Kang Shih. Probing critical point energies of transition metal dichalcogenides: surprising indirect gap of single layer wse2. *Nano letters*, 15(10):6494–6500, 2015.

[35] Haotian Wang, Desheng Kong, Petr Johanes, Judy J Cha, Guangyuan Zheng, Kai Yan, Nian Liu, and Yi Cui. Mose2 and wse2 nanofilms with vertically aligned molecular layers on curved and rough surfaces. *Nano letters*, 13(7):3426–3433, 2013.

[36] Yilei Li, Alexey Chernikov, Xian Zhang, Albert Rigosi, Heather M Hill, Arend M van der Zande, Daniel A Chenet, En-Min Shih, James Hone, and Tony F Heinz. Measurement of the optical dielectric function of monolayer transition-metal dichalcogenides: Mos 2, mo s e 2, ws 2, and ws e 2. *Physical Review B*, 90(20):205422, 2014.

[37] Ashish Arora, Karol Nogajewski, Maciej Molas, Maciej Koperski, and Marek Potemski. Exciton band structure in layered mose 2: from a monolayer to the bulk limit. *Nanoscale*, 7(48):20769–20775, 2015.

[38] Ashish Arora, Karol Nogajewski, Maciej Molas, Maciej Koperski, and Marek Potemski. Exciton band structure in layered mose 2: from a monolayer to the bulk limit. *Nanoscale*, 7(48):20769–20775, 2015.

[39] AR Beal, JC Knights, and WY Liang. Transmission spectra of some transition metal dichalcogenides. ii. group via: trigonal prismatic coordination. *Journal of Physics C: Solid State Physics*, 5(24):3540, 1972.

[40] Won Seok Yun, S. W. Han, Soon Cheol Hong, In Gee Kim, and J. D. Lee. Thickness and strain effects on electronic structures of transition metal dichalcogenides: 2h-mX_2 semiconductors ($\mathrm{m} =$ mo, w; $\mathrm{x} =$ s, se, te). *Phys. Rev. B*, 85:033305, Jan 2012.

[41] Nourdine Zibouche, Agnieszka Kuc, Janice Musfeldt, and Thomas Heine. Transition-metal dichalcogenides for spintronic applications. *Annalen der Physik*, 526(9-10):395–401, 2014.

[42] Weijie Zhao, Zohreh Ghorannevis, Leiqiang Chu, Minglin Toh, Christian Kloc, Ping-Heng Tan, and Goki Eda. Evolution of electronic structure in atomically thin sheets of ws2 and wse2. *ACS nano*, 7(1):791–797, 2012.

[43] A Carvalho, RM Ribeiro, and AH Castro Neto. Band nesting and the opti-

cal response of two-dimensional semiconducting transition metal dichalcogenides. *Physical Review B*, 88(11):115205, 2013.

[44] G Wang, IC Gerber, L Bouet, D Lagarde, A Balocchi, M Vidal, T Amand, X Marie, and B Urbaszek. Exciton states in monolayer mose2: impact on interband transitions. *2D Materials*, 2(4):045005, 2015.

[45] JA Reyes-Retana and F Cervantes-Sodi. Spin-orbital effects in metal-dichalcogenide semiconducting monolayers. *Scientific reports*, 6:24093, 2016.

[46] Suresh Vishwanath, Aditya Sundar, Xinyu Liu, Angelica Azcatl, Edward Lochocki, Arthur R Woll, Sergei Rouvimov, Wan Sik Hwang, Ning Lu, Xin Peng, et al. Mbe growth of 2h-mote2 and 1t'-mote2 on 3d substrates. *arXiv preprint arXiv:1705.00651*, 2017.

[47] Claudia Ruppert, Ozgur Burak Aslan, and Tony F Heinz. Optical properties and band gap of single-and few-layer mote2 crystals. *Nano letters*, 14(11):6231–6236, 2014.

[48] TMG Mohiuddin, A Lombardo, RR Nair, A Bonetti, G Savini, R Jalil, Nicola Bonini, DM Basko, C Galiotis, N Marzari, et al. Uniaxial strain in graphene by raman spectroscopy: G peak splitting, grüneisen parameters, and sample orientation. *Physical Review B*, 79(20):205433, 2009.

[49] Zhen Hua Ni, Ting Yu, Yun Hao Lu, Ying Ying Wang, Yuan Ping Feng, and Ze Xiang Shen. Uniaxial strain on graphene: Raman spectroscopy study and band-gap opening. *ACS nano*, 2(11):2301–2305, 2008.

[50] David Lloyd, Xinghui Liu, Jason W Christopher, Lauren Cantley, Anubhav Wadehra, Brian L Kim, Bennett B Goldberg, Anna K Swan, and J Scott Bunch. Band gap engineering with ultralarge biaxial strains in suspended monolayer mos2. *Nano Letters*, 16(9):5836–5841, 2016.

[51] Andres Castellanos-Gomez, Rafael Roldán, Emmanuele Cappelluti, Michele Buscema, Francisco Guinea, Herre SJ van der Zant, and Gary A Steele. Local strain engineering in atomically thin mos2. *Nano letters*, 13(11):5361–5366, 2013.

[52] Timo Schumann. Dissertation, doctor rerum naturalim (dr. rer. nat.). 2014.

[53] Fumihiko Maeda and Hiroki Hibino. Thin graphitic structure formation

on various substrates by gas-source molecular beam epitaxy using cracked ethanol. *Japanese Journal of Applied Physics*, 49(4S):04DH13, 2010.

[54] DG Mead and JC Irwin. Raman spectra of sns 2 and snse 2. *Solid State Communications*, 20(9):885–887, 1976.

[55] Kleopatra Emmanouil Aretouli, Dimitra Tsoutsou, Polychronis Tsipas, Jose Marquez-Velasco, Sigiava Aminalragia Giamini, Nicolaos Kelaidis, Vassilis Psycharis, and Athanasios Dimoulas. Epitaxial 2d snse2/2d wse2 van der waals heterostructures. *ACS Applied Materials & Interfaces*, 8(35):23222–23229, 2016.

[56] Peng Yu, Xuechao Yu, Wanglin Lu, Hsin Lin, Linfeng Sun, Kezhao Du, Fucai Liu, Wei Fu, Qingsheng Zeng, Zexiang Shen, et al. Fast photoresponse from 1t tin diselenide atomic layers. *Advanced Functional Materials*, 26(1):137–145, 2016.

[57] E Xenogiannopoulou, P Tsipas, KE Aretouli, D Tsoutsou, SA Giamini, C Bazioti, GP Dimitrakopulos, Ph Komninou, Steven Brems, Cedric Huyghebaert, et al. High-quality, large-area mose 2 and mose 2/bi 2 se 3 heterostructures on aln (0001)/si (111) substrates by molecular beam epitaxy. *Nanoscale*, 7(17):7896–7905, 2015.

[58] Joseph M Gonzalez and Ivan I Oleynik. Layer-dependent properties of sns 2 and snse 2 two-dimensional materials. *Physical Review B*, 94(12):125443, 2016.

[59] BT Kelly. The thermal expansion coefficients of graphite crystalsthe theoretical model and comparison with 1990 data. *Carbon*, 29(6):721–724, 1991.

[60] BT Kelly and MJ Duff. On the validity of lennard-jones potentials for the calculation of elastic properties of a graphite crystal. *Carbon*, 8(1):77–83, 1970.

[61] JF Green, P Bolsaitis, and IL Spain. Pressure dependence of c-axis elastic parameters of oriented graphite. *Journal of Physics and Chemistry of Solids*, 34(11):1927–1937, 1973.

[62] BT Kelly and PL Walker. Theory of thermal expansion of a graphite crystal in the semi-continuum model. *Carbon*, 8(2):211–226, 1970.

[63] SH El-Mahalawy and BL Evans. The thermal expansion of 2h-mos2, 2h-

mose2 and 2h-wse2 between 20 and 800 c. *Journal of Applied Crystallography*, 9(5):403–406, 1976.

[64] Toshihiro Shimada, Hiroyuki Nishikawa, Atsushi Koma, Yukito Furukawa, Etsuo Arakawa, Kunikazu Takeshita, and Ta-i Matsushita. Polytypes and crystallinity of ultrathin epitaxial films of layered materials studied with grazing incidence x-ray diffraction. *Surface science*, 369(1-3):379–384, 1996.

[65] Toshihiro Shimada, Yukito Furukawa, Etsuo Arakawa, Kunikazu Takeshita, Tadashi Matsushita, Hideki Yamamoto, and Atsushi Koma. Structure determination of ultrathin nbse2 films by grazing incidence x-ray diffraction. *Solid state communications*, 89(7):583–586, 1994.

[66] RF Brebrick. Partial pressure of se2 (g) in selenium vapor. *The Journal of Chemical Physics*, 48(12):5741–5743, 1968.